International Journal of Coal Science & Technology (2023) 10:33
https://doi.org/10.1007/s40789-023-00591-8

RESEARCH

Spectral narratives of microstructural restyling and their controls on hydrocarbon generation potential from coal

Tushar Adsul[1] · Santanu Ghosh[1,2] · Anwita Ojha[1] · Sudip Bhattacharyya[3] · Atul Kumar Varma[1]

Received: 13 September 2022 / Revised: 20 February 2023 / Accepted: 9 May 2023

Abstract

The low to medium-rank Tertiary coals from Meghalaya, India, are explored for the first time for their comprehensive microstructural characterization using the FTIR and Raman spectroscopy. Further, results from these coals are compared with the Permian medium and high-rank coals to understand the microstructural restyling during coalification and its controls on hydrocarbon generation. The coal samples are grouped based on the mean random vitrinite reflectance values to record the transformations in spectral attributes with increasing coal rank. The aliphatic carbon and the apparent aromaticity respond sharply to the first coalification jump ($\bar{R}_r$: 0.50%) during low to medium-rank transition and anchizonal metamorphism of the high-rank coals. Moreover, the Raman band intensity ratio changes during the first coalification jump but remains invariable in the medium-rank coals and turns subtle again during the onset of pregraphitization in high-rank coals, revealing a polynomial trend with the coal metamorphism. The Rock–Eval hydrogen index and genetic potential also decline sharply at the first coalification jump. Besides, an attempt to comprehend the coal microstructural controls on the hydrocarbon potential reveals that the Tertiary coals comprise highly reactive aliphatic functionalities in the type II-S kerogen, along with the low paleotemperature (74.59–112.28 °C) may signify their potential to generate early-mature hydrocarbons. However, the presence of type II-III admixed kerogen, a lesser abundance of reactive moieties, and overall moderate paleotemperature (91.93–142.52 °C) of the Permian medium-rank coals may imply their mixed hydrocarbon potential. Meanwhile, anchizonal metamorphism, polycondensed aromatic microstructure, and high values of paleotemperature (~ 334.25 to ~ 366.79 °C) of the high-rank coals indicate a negligible potential of producing any hydrocarbons.

Keywords Early mature oil generation · Meghalaya high-sulfur coal · Type II-S kerogen · Microstructural ordering · Coalification jump · Hydrocarbon generation potential

1 Introduction

Coal microstructure is utterly sensitive to geological events and thus, provides the key to unveil the paleoevents that affect the organic matter (OM). One of the factors affecting the microstructural properties of coal is the pronounced jump in coalification during the evolution of coal. The first coalification jump is characterized by sharp changes in coal properties during the early stages of coalification (Bustin and Guo 1999). Notably, it involves the gradual depletion of oxygen-containing structures and aliphatic side chains from the macromolecular matrix of coal (Xin et al. 2022). In an attempt to understand the effects of coalification on the molecular structure of coal, Jiang et al. (2019) reported the microstructural amendments in coal during the first coalification jump at $\bar{R}_r$: 0.50%. These changes include a gradual increase in aromatic rings at the expense of declining

✉ Atul Kumar Varma
atul@iitism.ac.in

1 Coal Geology and Organic Petrology Laboratory, Department of Applied Geology, Indian Institute of Technology (Indian School of Mines), Dhanbad, Jharkhand 826004, India

2 Department of Geology, Mizoram University, Aizawl, Mizoram 796004, India

3 Specialized Coal Petrography Laboratory, Natural Energy Resources, Mission II-B, Geological Survey of India, DK-6, Sector-II, Salt Lake City, Kolkata, West Bengal 700091, India

Published online: 16 June 2023

aliphatic side chains. Further, previous authors have recognized a lower threshold reflectance value for the first coalification jump at $\bar{R}_r$: 0.50% (Zhou et al. 2017, 2018, Tao et al. 2018). Moreover, the generally accepted oil generation threshold at $\bar{R}_r$: 0.50% was successfully tested by Yao et al. (2006) using laboratory simulation experiments and attributed this range to a first coalification jump.

Investigations revealed that the chemical and molecular framework of coal is highly complex in nature (Baysal et al. 2016). Therefore, the heterogenic properties and complex internal structure pose many challenges to the structural and chemical characterization of coal (Saikia et al. 2009; Jiang et al. 2019, 2021). Nevertheless, it is worth noting that the chemical framework and the molecular structure of the low to medium-rank coals play significant roles in various coal conversion processes, including coal gasification (Baysal et al. 2016), coal liquefaction (Baysal et al. 2016), and coal combustion (Zhou et al. 2012; Liu et al. 2016). Therefore, despite difficulties, it is imperative to study the chemical framework and the micromolecular structure of these coals to be familiar with the various factors of coal conversion. A large number of chemical and structural parameters of coal, i.e., functional group chemistry, degree of microstructural crystallinity, heteroatomic heterogeneity, and molecular structures, can be obtained from highly sensitive and advanced analytical techniques, such as the vitrinite reflectance analysis, Fourier transform infrared (FTIR), and Raman spectra to address those challenges. The FTIR spectra depict stretching and bending vibrations of the organic molecules and the chemical bonds of the mineral matter to document the types of kerogen, thermal maturity, and evolution of chemical framework with the rank advancement of carbonaceous materials (Orrego-Ruiz et al. 2011; Chen et al. 2012; Hazra et al. 2015; Okolo et al. 2015; Misra et al. 2019; Biswas et al. 2020; Ghosh et al. 2020). Besides, owing to its sensitivity to the crystalline and amorphous structures of carbonaceous materials, Raman spectroscopy finds a wide array of applications in the characterization of carbon-based materials (Beyssac et al. 2002a, 2002b; Sadezky et al. 2005; Marques et al. 2009; Kwiecińska et al. 2010; Rodrigues et al. 2011; Morga et al. 2015; Baysal et al. 2016; Lünsdorf 2016; Xueqiu et al. 2017; Henry et al. 2018, 2019a, 2019b; Khatibi et al. 2018). Additionally, the Rock–Eval pyrolysis, commonly used to assess source rock hydrocarbon potential, is also applied here to support the transformations during the coalification stages.

The study area in northeastern India comprises a considerable amount of low to medium-rank high-sulfur coal deposits (1,623.65 million tonnes, GSI 2019). Recently, these coal deposits have gained wide attention for various coal conversion processes due to their high-grade, low moisture, low ash yield (Khare and Baruah 2010; Mishra et al. 2014; Oliveira et al. 2014), and perhydrous nature at places (Chandra et al. 1983). However, due to the existing knowledge gap regarding the comprehensive microstructural framework of these north-east Indian coals, their complete characterization and utilization in coal conversion processes are in their infancy**.** Therefore, the objective of this study is to undertake a composite approach from different spectral probes to report more inclusive information about the internal structure of these coals, which may facilitate their academic and industrial utilization. To carry out this objective, the high-sulfur coals from Meghalaya, northeast India, are researched from a combined multispectral approach for the first time to appraise the microstructure and its plausible influences on hydrocarbon generation, which defines the novelty of this investigation. Further, to portray the whims of microstructural restyling with coalification, these coals are compared with the medium and high-rank coals from the Jharia and the Raniganj Basins and the Rangit tectonic window, Sikkim Himalaya, India, respectively. Different spectral attributes and semi-quantitative spectral ratios (ID_1/IG, FWHM of the G and the D_1 bands, Raman band separation, and "A-factor") are calculated to delve deep into the chemical functionalities present in these coals and their roles in hydrocarbon generation. This investigation has a wider scope in the application of the northeast Indian coals in nanoproducts synthesis, coal liquefaction, coal gasification, hydrocarbon exploration, enhanced kerogen pyrolysis, and developing any strategy for sulfur removal for their better utilization.

2 Geological setting

The Meghalaya plateau (20°01′ N to 26°05′ N; 85°49′ E to 92°53′ E) is a rigid Precambrian cratonic block (Fig. 1a) at the northeastern extremity of India. It covers an area of 22,429 km^2. It is structurally a horst and is bordered by the Brahmaputra lineament to the north, dextrally moving Dauki fault to the south, the Naga-Disang thrusted schuppen belt to the east and the Dhubri-Yamuna lineament to the west. The Eocene coal deposits of Meghalaya (Chandra et al. 1983) formed on the platform basin peripheral to the Shillong plateau under stable shelf conditions (Mishra and Ghosh 1996).

The general stratigraphy of Meghalaya is portrayed in Fig. 1b. The coal deposits of Meghalaya form a narrow belt from the Garo hills (West Darrangiri and Siju coal basins) in the west through the Khasi hills (Langrin and Mawlong-Shella coal basins) in the middle to the Jaintia Hills in the east (Fig. 1c) (Chandra et al. 1983). There are other minor coal basins, such as Laitryngew, Cherrapunji, and Bapung. Coal deposits occur on the platform area within the Tertiary system of the Eocene age. The coal-bearing horizons include carbonaceous shale and grey shale striking NNW-SSE to NE-SW to WSW-ENE,

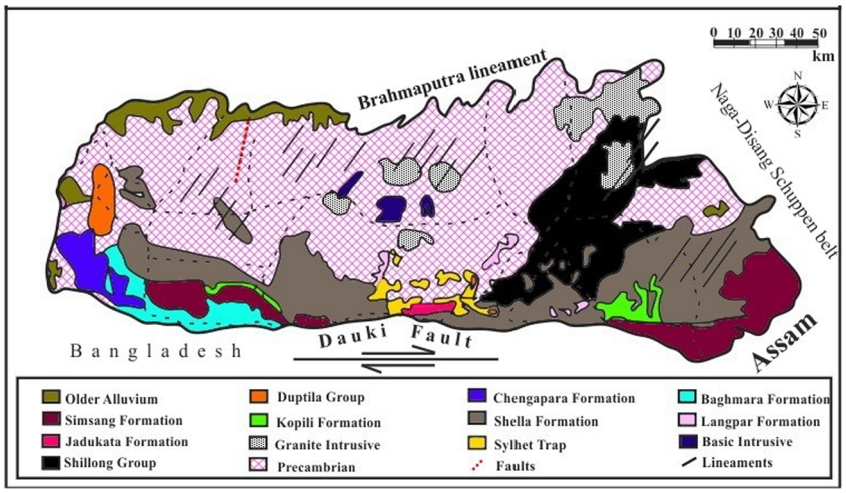

a

Age	Group	Formation	Member		Thickness (m)	Litho-units	Lithology
Oligocene		Simsang			1150		Medium to fine grained sandstone with intercalations of shale and siltstone
Early Oligocene to Late Oliogcene		Kopili			500		Ferruginous sandstone, pyritous splintery shale and grey siltstones
Middle Eocene	Jaintia	Sylhet Limestone	Prang Limestone/ Siju Limestone		60-150		Bluish Limestone with thinly bedded to massive appearance and marly interbeds (rich in foraminifera)
Late Eocene			Nurpuh Sandstone	These members also called Tura Fm. in West Khasi and Garo Hills.	15-26		Medium to coarse grained ferruginous sandstones intercalated with sandy limestone
			Umlatdoh Limestone		70-110		Grey limestone with pinkish tint, calcareous sandstone and sandy limestone (rich in foraminifera)
Late Eocene to Paleocene			Lakadong Sandstone		35-250		Medium grained and buff coloured arkosic sandstone with intercalations of thin coal seams and carbonaceous shale
Early Eocene to Paleocene			Lakadong Limestone		25-60		Brownish grey to grey coloured siliceous limestone
Early Eocene to Late Paleocene		Therria Sandstone			20-80		Medium to coarse grained buff coloured arkosic sandstone with thin pyritic bands and rich silty sandstons
Early Cretaceous to Early Paleocene		Langpar			10-50		Earthy limestones and calcareous ferruginous sandstones
Late Cretaceous		Mahadek			160-335		Massive and coarse textured glauconitic sandstones with calcareous horizons and dark greyish shale
Unconformity							
Jurassic to Lower Cretaceous			Sylhet Trap		250-400		Pahoehoe and Aa basaltic flow

b

Fig. 1 **a** The tectonic map of Meghalaya after Singh and Singh (2000) and Singh et al. (2021). **b** Stratigraphic succession of the Raja Rao (1981), Meghalaya after Misra (1992), Mishra and Ghosh (1996), and Singh and Singh (2000). **c** Study area after Swer and Singh (2003), Khare and Baruah (2010), and Talukdar et al. (2016) with the tentative locations of the sampling sites

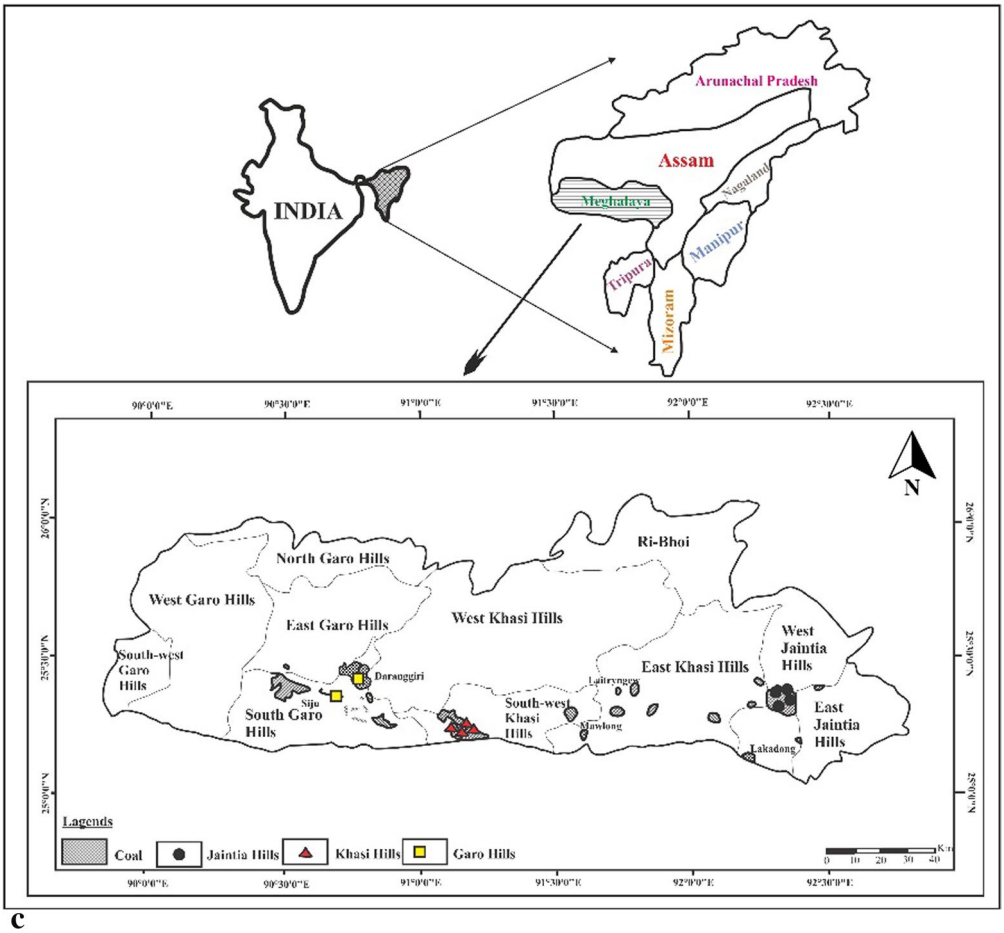

Fig. 1 (continued)

and these are either sub-horizontal or have a slight dip (~2°) toward the southwest. In places, the beds are almost horizontal. More information about the lithology and the relevant coal seam of a particular sample is furnished in Fig. 1b and Table 2, respectively.

The petrographic characterization of Meghalaya coals was carried out a little by previous workers (Ahmed and Bharali 1985; Goswami 1985). These coals are usually rich in vitrinite, followed by appreciable quantities of liptinite group macerals with a low concentration of inertinite macerals (Mishra and Ghosh 1996). Singh and Singh (2000) demonstrated the deposition facies of these coal seams based on the petrographic models. According to them, the Jaintia Hills coals were formed under recurrent marine incursion events. In contrast, the Khasi Hills coals predominantly formed under telmatic to limno-telmatic conditions, and the coals of Garo Hills formed in reed swamps in telmatic to limnic conditions. Further, Misra (1992) advocated that the Meghalaya peat swamps developed on the fringe of the stable shelf with intermittent marine transgression events.

3 Material and methods

3.1 Sample collection and preparation

The studied low to medium-rank coal samples from northeast India belong to the Jaintia, Khasi, and Garo Hills of the eastern, middle, and western Meghalaya, respectively (Fig. 1c). Twenty-two (22) coal samples were accumulated from the Jaintia, Khasi, and Garo Hills of Meghalaya, Raniganj and Jharia Basins of West Bengal, and Jharkhand, and the Rangit tectonic window of the Sikkim Himalaya, India. The collected fresh samples were cleaned for recent sediment and dust particles to avoid contamination. The samples were immediately stored in clean and air-locked bags to protect them from unnecessary moisture and dust. Manual mixing of coal samples was done with due care to alleviate sample segregation. Then, the manual method was undertaken for the division of coal samples using the flattened-heap method according to the ISO 18283 (2006) standard. The detailed sampling of medium-rank coals from the Jharia and the Raniganj Basins and the high-rank

coals from the Rangit tectonic window are outlined in the works of Ghosh et al. (2018, 2020).

3.2 Elemental properties of coal samples

Carbon, hydrogen, nitrogen, sulfur, and oxygen (CHNSO) distributions of the coals were analyzed on -212 micron-sized grains at the Spectroscopy and Analytical Test Facility, Indian Institute of Science (IISc), Bangalore, India, following the guidelines of ASTM (2015). Thermo scientific flash 2000 organic elemental analyzer was employed under the CHNS/O mode for the elemental analysis. The furnace temperature was set at 900 °C and 1060 °C for CHNS and oxygen, respectively, for complete flash combustion using helium as a carrier gas. The combustion products were allowed to pass through the gas chromatography (GC) column at 75 °C for CHNS and 100 °C for oxygen to be separated by the retention rates. Finally, the gases were detected at the thermal conductivity detector (TCD) to produce chromatographs. After integrating the curves, the carbon, hydrogen, nitrogen, sulfur, and oxygen concentrations were quantified in weight percentages.

3.3 Vitrinite reflectance measurements

For vitrinite reflectance measurements, the coal samples were air-dried at 40 °C for approximately 3 h following the ISO 18283 (2006) guidelines. The samples were then manually crushed and passed through a sieve with an opening of 1 mm following ISO 3310-1 (2000). The coal pellets were prepared after mixing those sieved coal particles with the epoxy resin and binder. One face of each pellet was grounded and polished for reflectance measurements to get a scratch and relief-free surface following the protocols mentioned in ISO 7404-2 (2009a, 2009b). After the complete preparation of the pellets, they were dehydrated in a desiccator for 15 h before the vitrinite reflectance measurements.

Non-polarized light of wavelength (λ) 546 nm was directed to the ideal vitrinite grains of the coal pellets immersed in oil ($n_e = 1.518$ at 23 °C). The Leica DMRXP microscope with a photometer (PMT-III) attached with the MSP-200 software, and Leica Application Suite (LAS) was employed for the vitrinite reflectance analysis following the ISO 7404-5 (2009a, 2009b) standard. Random vitrinite reflectance values (100 counts) were obtained for each sample from which the mean reflectance ($\bar{R}r\%$) was calculated. The reflectance measurement of the Sikkim high-rank samples was performed by Ghosh et al. (2018). Further, Ghosh et al. (2020) elaborated on the reflectance measurement procedure and calculation of the $\bar{R}_r\%$ values of the medium-rank samples from the Jharia and the Raniganj Basins and high-rank samples from the Rangit tectonic window. The $\bar{R}_r\%$ values were used to calculate the peak paleotemperature of the Meghalaya coals following Eq. (1) from Barker and Pawlewicz (1994):

$$T_{\text{peak}} = \frac{\{\text{In}(\bar{R}r) + 1.68\}}{0.0124} \quad (1)$$

Further, the paleotemperature of the medium-rank samples from the Jharia and the Raniganj Basins and high-rank samples (Rangit tectonic window) were reported by Ghosh et al. (2020).

3.4 Fourier transform infrared (FTIR) spectroscopy

The sample preparation for the FTIR spectroscopy was performed following Painter et al. (1981). A total of 32 infrared scans were recorded at a resolution of 4 cm^{-1} within the scan range of 4000–400 cm^{-1}. The Vertex 80 FTIR system

Table 1 Calculations of the FTIR parameters following Ganz and Kalkreuth (1987), Ibarra et al. (1994), Guo and Bustin (1998), Chen et al. (2012), Xueqiu et al. (2017), Jiang et al. (2019), and Liu et al. (2019)

Semi-quantitative FTIR parameters	Calculations	Band region (cm^{-1})	Equation no
Apparent aromaticity (f_a)	$\frac{H_{al}}{H} = \frac{H_{al}}{H_{al}+H_{ar}}$	$\frac{H_{al}}{H} = \frac{A_{3000-2800}}{(A_{3000-2800}+A_{900-700})}$	(2)
	$\frac{C_{al}}{C} = \frac{\frac{H_{al}}{H} * \frac{H}{C}}{\frac{H_{al}}{C_{al}}}$	$\frac{C_{al}}{C} = \frac{\frac{A_{3000-2800}}{(A_{3000-2800}+A_{900-700})} * \frac{H}{C}}{1.8}$	(3)
	$f_a = 1 - \frac{C_{al}}{C}$	$f_a = 1 - \frac{\frac{A_{3000-2800}}{(A_{3000-2800}+A_{900-700})} * \frac{H}{C}}{1.8}$	(4)
"A-factor"	$\frac{CH_{al(stretching)}}{(CH_{al(stretching)}+C{=}C_{stretching})}$	$\frac{A_{3000-2800}}{(A_{3000-2800}+A_{1600})}$	(5)
"C-factor"	$\frac{C{=}O}{(C{=}O+C{=}C)}$	$\frac{A_{1750-1650}}{(A_{1750-1650}+A_{1600})}$	(6)

Explanations: H_{al}/H is the ratio of the concentrations of aliphatic hydrogen (H_{al}) to the total hydrogen atoms (H). C_{al}/C represents the aliphatic carbon fraction. H/C represents the atomic ratio of hydrogen to carbon, calculated from the ultimate analysis. H_{al}/C_{al} is the proportion of hydrogen and carbon in aliphatic groups that is already pre-defined for coals at 1.8 (Ibarra et al. 1994; Xueqiu et al. 2017). "A-factor" and "C-factor" are the indicators of hydrocarbon generation potential and coal maturation, respectively (Ganz and Kalkreuth 1987). 'A' denotes the area of the band region or a particular peak

coupled with a Bruker 3000 Hyperion Microscope was employed at the Sophisticated Analytical Instrument Facility (SAIF) in the Indian Institute of Technology, Bombay (IIT-B), India. The spectral deconvolution and fitting using the Gaussian function were performed in the Fityk 1.3.1 software. The formulations of the semi-quantitative parameters from the fitted FTIR spectra are furnished in Table 1.

3.5 Raman spectroscopy

The Raman spectroscopy of ten (10) low to medium-rank samples of Meghalaya was carried out at the Sophisticated Analytical Instrument Facility (SAIF) in the Indian Institute of Technology, Bombay (IIT-B), India. The Horiba Jobin Yvon HR-800 UV confocal Micro-Raman spectrometer recorded the Raman signals on the powdered coal samples. The 532 nm laser source at the resolution of 1800 lines/mm was used. Each sample was scanned for about 10 s from 1000 to 2000 cm^{-1} region. Three spectra of individual samples were measured, and the mean values of the Raman signals and spectral intensities were computed. The final spectrum was fitted using the Gaussian function in the Fityk 1.3.1 software. Meanwhile, Ghosh et al. (2018) and Ghosh et al. (2020) reported the Raman spectral deconvolution features of the medium-rank coals from the Raniganj and Jharia Basins and high-rank samples from Sikkim, respectively.

3.6 Rock–Eval pyrolysis

A Rock–Eval 6 pyrolyzer was employed to evaluate the source rock characteristics of the studied coals following the methodologies furnished by Varma et al. (2015) at the Keshava Deva Malaviya Institute of Petroleum Exploration (KDMIPE, ONGC, India). The assessed parameters include total organic carbon (TOC) content, thermolabile hydrocarbons under the S1 curve, thermally cracked pyrolyzates under the S2 curve, and the temperature that promotes peak thermal cracking of kerogen and release of maximum amounts of hydrocarbons (T_{max}), hydrogen index $\{HI = 100 \times (S2/TOC)\}$, and bulk hydrocarbon genetic potential ($GP = S1 + S2$) of kerogen.

4 Results and discussions

4.1 Coal properties

The general coal characteristics, including the technological parameters, elemental distributions, atomic ratios, vitrinite reflectance measurements, and calculated peak paleotemperature values are presented in Table 2. The rank of the Meghalaya coal samples ranges from Lignite B, subbituminous, Bituminous D to Bituminous C, whereas the Jharia and the Raniganj coals fall in the Bituminous C to Bituminous B category. Further, the high-rank coals belong to Anthracite A following ISO 11760:2005 rank classification standard. The Meghalaya coals are low in moisture and ash yield; therefore, these coals are considered high-grade for various coal beneficiation processes (Khare and Baruah 2010). Further, the volatile matter yield range and low moisture and ash yield values may impart semi-coking characteristics to these coals. The decline in the average volatile matter yield from the Meghalaya coals through the Raniganj and the Jharia coal to the Sikkim Anthracites suggests an increase in the rank of these coals. Similarly, an increase in the fuel ratio implies a rank increment from the Meghalaya to Sikkim coals. Additionally, carbon content on a dry ash-free basis (^{daf}) corroborates with the fuel ratio to estimate the rank of the studied samples (Table 2).

The ultimate analysis depicts that the studied low to medium-rank coal samples from Meghalaya are rich in total sulfur content along with high oxygen and hydrogen contents. The decarboxylation, decarbonylation, demethylation, and dehydroxylation reactions alleviate the oxygen and hydrogen contents with increasing coal metamorphism (Killops and Killops 2005). Therefore, the large oxygen and hydrogen contents in studied low to medium-rank coals of Meghalaya and medium-rank coals from the Jharia and the Raniganj Basins may indicate that these reactions have not significantly altered the chemical compositions of these coals yet and hence, suggest that these samples have experienced a low to moderate burial temperature (calculated from Eq. (1); see Sect. 4.2) and belong to the lower metamorphic grade hitherto.

Markedly, the large total sulfur content in the Meghalaya coal samples is likely due to the marine incursion to the peat-forming mires or strong alkaline environment in a marginal-marine setting. Further, the van-Krevelen diagram constructed by the atomic H/C versus O/C ratio reveals that these samples comprise type II-S kerogen (Fig. 2). This type of kerogen comprises a large number of alkyl chains associated with the kerogen nuclei by the S–S and the C–S bonds. These bonds have lower bond dissociation energy than the C–O and the C–C bonds, which dominate the chemical frameworks of other kerogen types. Due to the presence of these weaker bonds and, therefore, reactive chemical framework, type II-S kerogen can expel hydrocarbons at a considerably lower temperature than the other kerogen types (Orr 1986) (except the type I kerogen). Further, the Raniganj and the Jharia coal samples on the van-Krevelen diagram portray type II-III admixed kerogen. This kerogen combination may produce a mixed type of hydrocarbons (oil and gas) depending upon the extent of maturity (Killlops and Killops 2005).

Table 2 Technological and elemental properties of the studied coal samples

Sample ID	Location	Coal seam	$\bar{R}_r$ (%)	T_{peak} (°C)	Rank	W^a (wt.%)	VM^a (wt.%)	A^a (wt.%)	FC (wt.%)	VM^{daf} (wt.%)	A^{db} (wt.%)	FR	C^{daf} (wt.%)	H^{daf} (wt.%)	N^{daf} (wt.%)	S^{daf} (wt.%)	O^{daf} (wt.%)	O/C	H/C
CG-5213	Jaintia Hills	Bapung main seam	0.26	–	Lignite B	8.40	40.10	11.92	39.58	50.33	13.01	0.99	82.73	6.09	1.00	4.70	5.48	0.05	0.88
CG-5219	Khasi Hills	Langrin main seam	0.47	74.59	Sub-bituminous	3.90	42.50	3.80	49.80	46.05	3.95	1.17	79.64	6.39	0.83	4.08	9.06	0.09	0.96
CG-5209	Jaintia Hills	Bapung main seam	0.48	76.29	Sub-bituminous	3.30	36.80	21.21	38.69	48.75	21.94	1.05	74.51	5.29	1.47	8.57	10.16	0.10	0.85
CG-5214	Jaintia Hills	Bapung main seam	0.53	84.28	Bituminous D	1.40	31.30	25.20	42.10	42.64	25.56	1.34	80.55	5.50	0.88	4.68	8.40	0.08	0.81
CG-5221	Khasi Hills	Langrin main seam	0.57	90.15	Bituminous D	3.90	39.00	25.00	32.10	54.85	26.01	0.82	61.18	5.02	1.51	16.82	15.47	0.19	0.98
CG-5227	Garo Hills	Daranggiri main seam	0.57	90.15	Bituminous D	5.60	40.60	5.41	48.39	45.62	5.73	1.19	79.02	6.26	1.03	2.54	11.15	0.11	0.94
CG-5223	Khasi Hills	Langrin main seam	0.58	91.55	Bituminous D	2.30	25.70	36.60	35.40	42.06	37.46	1.38	74.74	6.53	2.03	3.78	12.92	0.13	1.04
CG-5229	Garo Hills	Daranggiri main seam	0.59	92.93	Bituminous D	5.40	40.70	6.91	46.99	46.42	7.31	1.15	78.63	5.89	0.90	5.83	8.75	0.08	0.89
CG-5217	Khasi Hills	Langrin main seam	0.60	94.29	Bituminous D	3.50	40.50	7.60	48.40	45.56	7.88	1.20	80.05	5.96	0.76	3.14	10.09	0.09	0.89
CG-5204	Jaintia Hills	Bapung main seam	0.75	112.28	Bituminous C	2.80	36.00	6.20	55.00	39.56	6.38	1.53	79.86	6.28	0.72	5.79	7.35	0.07	0.94
CG-1672	Raniganj	Kuardih, Seam #14	0.58	91.93	Bituminous C	4.00	31.33	18.00	46.67	40.17	18.75	1.49	76.86	5.08	1.68	1.63	14.75	0.14	0.79
CG-1671	Raniganj	Rotibati G4	0.65	100.64	Bituminous C	4.90	30.83	14.57	49.70	38.28	15.32	1.61	78.46	5.58	1.89	0.55	13.52	0.13	0.85
CG-1676	Jharia	XIV seam	0.76	113.69	Bituminous C	0.97	32.10	21.00	45.93	41.13	21.21	1.43	80.38	5.49	2.24	0.83	11.06	0.10	0.81
CG-1675	Jharia	IX top seam	0.90	127.09	Bituminous C	1.00	21.13	29.77	48.10	30.50	30.07	2.28	82.25	4.84	1.79	0.75	10.37	0.09	0.70
CG-1673	Jharia	BP seam	0.95	131.68	Bituminous C	2.00	28.84	13.97	55.19	34.32	14.26	1.91	88.89	4.94	2.04	0.65	3.48	0.03	0.66
CG-1677	Jharia	Salaspur C seam	1.00	135.58	Bituminous C	0.99	29.82	15.97	53.22	35.91	16.13	1.79	84.90	5.11	2.12	0.96	6.91	0.06	0.72
CG-1679	Jharia	Gopinathpur bottom seam	1.00	135.58	Bituminous C	0.98	23.75	27.40	47.87	33.15	27.67	2.02	83.92	4.91	1.63	0.91	8.63	0.08	0.70
CG-1674	Jharia	VII bottom seam	1.09	142.52	Bituminous B	1.90	16.90	28.54	52.66	24.30	29.09	3.12	84.04	4.66	1.70	0.85	8.75	0.08	0.66
CG-3305	Reshi	Not known	4.15	334.25	Anthracite A	3.75	7.87	50.27	38.10	17.12	52.23	4.84	89.11	1.72	1.22	–	7.95	0.07	0.23
CG-3306	Reshi	Not known	4.73	350.87	Anthracite A	2.97	6.85	49.02	41.16	14.27	50.52	6.01	93.63	1.30	0.40	–	4.67	0.04	0.17
CG-3300	Jorethang	Not known	5.12	361.07	Anthracite A	2.21	2.80	50.55	44.44	5.93	51.69	15.86	94.14	1.52	0.46	–	3.88	0.03	0.19
CG-3303	Namchi	Not known	5.36	366.79	Anthracite A	2.73	5.32	50.97	40.97	11.50	52.40	7.70	87.74	2.67	1.53	–	8.06	0.07	0.36

Explanations: $\bar{R}_r$ % = Mean random vitrinite reflectance; T_{peak} = Maximum temperature of burial heating calculated using equations of Barker and Pawlewicz (1994); The values for $\bar{R}_r$ % and paleotemperature for medium-rank coals from the Jharia and the Raniganj Basins and high-rank coals from the Sikkim, India are reported from Ghosh et al. (2020), and reuse of the data is permitted by the Elsevier and Copyright Clearance center; Licence Number: 5215880419644; dated: 25th December 2021; W = Moisture content; VM = Volatile Matter yield; A = Ash yield; FC = Fixed Carbon content; FR = Fuel ratio; C = Carbon content; H = Hydrogen content; N = Nitrogen content; S = Sulfur content; O = Oxygen content; ^{a} = analytical state; ^{db} = dry basis; ^{daf} = dry ash free basis; '–' denotes that the equation (Barker and Pawlewicz 1994) is not valid for this particular reflectance value; The rank classification follows the ISO 11760:2005 standard

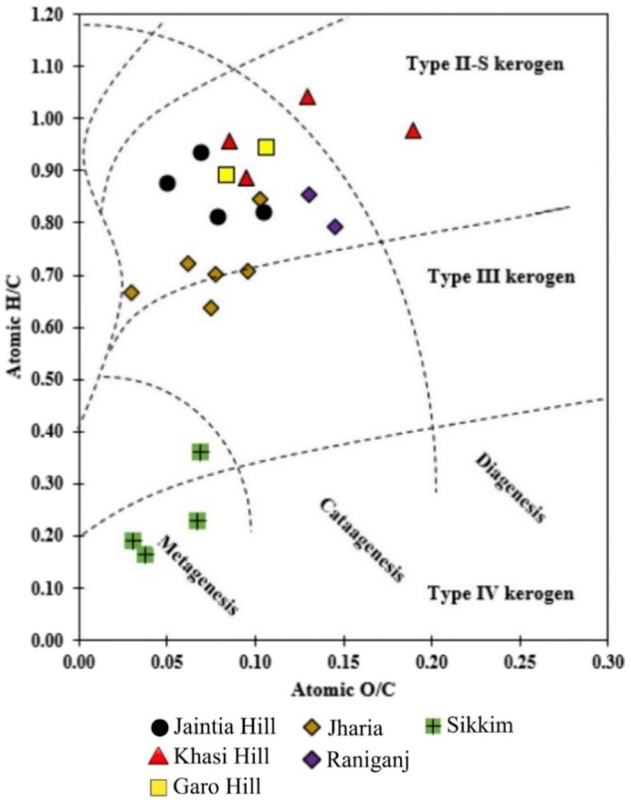

Fig. 2 Atomic H/C versus O/C (van-Krevelen) diagram

Hence, the studied low to medium-rank samples reveal significant hydrocarbon potential owing to their reactive chemical structure. On the other hand, the van-Krevelen plot and calculated peak paleotemperatures (see Sect. 4.2) of the high-rank samples from Sikkim suggest that these samples are at metagenesis to the post-metagenesis stage with a poor hydrocarbon generation potential.

4.2 Vitrinite reflectance, coal rank, and basinal paleotemperature

Based on the mean random vitrinite reflectance ($\bar{R}_r$%) values, the coal samples from Meghalaya are divided into two groups. The low-rank samples (< 0.40%–0.50%) comprise the lignite ($\bar{R}_r$: < 0.40%) and subbituminous ($\bar{R}_r$: 0.40%–0.50%) coals, while the medium-rank samples (> 0.50%–1.00%) include the bituminous D ($\bar{R}_r$: 0.50%–0.60%), and bituminous C ($\bar{R}_r$: 0.60%–1.00%) coals. Further, the Raniganj and the Jharia coals are categorized into medium-rank coals (0.58%–1.09%; Anwita et al. 2020; Ghosh et al. 2020) consisting of bituminous D ($\bar{R}_r$:0.50%–0.60%), bituminous C ($\bar{R}_r$: 0.60%–1.00%), and bituminous B ($\bar{R}_r$:1.00%–2.00%) rank (ISO 11760:2005). On the other hand, the Sikkim coal samples are grouped into high-rank coals ($\bar{R}_r$: 4.15%–5.36%; Anwita et al. 2020; Ghosh et al. 2018, 2020). The $\bar{R}_r$ value of 0.50% is set as the boundary between the low-rank and medium-rank coals following the concept of the 'first coalification jump.' Bustin and Guo (1999) suggested that among the four or five jumps, the first coalification jump usually occurs at the high volatile bituminous coal rank ($\bar{R}_r$:0.50%–0.60%). Meanwhile, as discussed in subSect. 4.1, the Meghalaya coal samples comprise type II-S kerogen, which is extremely reactive than the type II-III kerogen to produce hydrocarbons before the peak thermal cracking of bitumen. Hence, the authors propose that the coalification jump in these samples occurs at the $\bar{R}_r$ of 0.50%, which forms the base of the division between the low ($\bar{R}_r < 0.50\%$) and medium rank ($\bar{R}_r > 0.50\%$) coal samples.

The heating temperature of the sedimentary OM, such as coal, is controlled by the maximum burial temperatures and the duration of the heating on the extended geological time scale (Barker and Pawlewicz 1986). However, this duo has limitations to measure in cooled sedimentary environments because of the weak thermal imprints. In such cases, $\bar{R}_r$% functions as an indicator of the peak temperature reached in the system. The $\bar{R}_r$% was used by many authors to document the peak temperature experienced by the OM in various geological settings (Bostick et al. 1979; Barker and Goldstein 1990; Piedad-Sánchez et al. 2004; Ghosh et al. 2018; Ghosh et al. 2020; Misra et al. 2019). The maximum temperature (T_{peak}) of burial heating experienced by the OM in low to medium-rank coals of Meghalaya ranges from 74.59 to 112.28 °C. In contrast, the medium-rank coals from the Jharia and the Raniganj Basins underwent burial heating temperatures from 91.93 to 142.52 °C (Ghosh et al. 2020). On the other hand, for the high-rank samples from Sikkim, the calculated peak temperature fluctuates between 334.25 and 366.79 °C (Ghosh et al. 2020). The values of paleotemperature for low to medium-rank coals may suggest that these samples have experienced late pre-catagenetic to catagenetic and post-catagenetic (Fig. 2) thermal maturation. Taylor et al. (1998) suggested that the distinctive temperature for coalification of high-rank coals is from ~ 170 to 250 °C. However, the paleotemperature range of these high-rank coals from Sikkim is beyond this coalification temperature range, suggesting the influence of thermal metamorphism under tectonic stress (anchizonal metamorphism; Ghosh et al. 2018).

The organic micropetrography of the vitrinite (collotelinite) grains substantiates these microstructural transformations with the coal metamorphism (Additonal file 1: Fig. S1a-d). The collotelinite grains in the sub-bituminous and bituminous coals from Meghalaya, Raniganj, and Jharia barely show any optical anisotropy (Fig. 1a–b) as the aromatic lamellae within them have not developed any preferred orientation, yet, and consist terminal functional groups and

heteroatomic bridges. Only a transition from the bituminous D to bituminous C rank implies a small rise in the microstructural ordering. At this rank, the primary driving forces of coalification were the temperature and the burial depth. However, with the increasing metamorphism to the anthracite A rank, and consequent depletion of the functional groups, methyl chains, and branches, the aromatic layers experienced polycondensation. The temperature enhanced the aromaticity, while the tectonic shear stress reoriented the aromatic lamellae within the vitrinite grains. These polyaromatic lamellae (Basic Structural Units (BSUs)) are oriented perpendicularly to the maximum stress direction of the triaxial stress field induced by the Himalayan orogeny in the Sikkim fold-thrust belts. This preferred orientation of the BSUs in the vitrinite grains developed optical anisotropy quantified by the bireflectance (Fig. 1c–d). The reflectance of the vitrinite grains in the anthracite A samples was presented by the Reflectance Indicating Surface (RIS), its principal axes (R_{MAX}, R_{INT}, and R_{MIN}), and parameters (R_{am}, R_{ev}, and R_{st}). Intense tectonic deformation episodes also resulted in the biaxial negative optical texture of these vitrinite grains as observed from the relation between the maximum, intermediate, and minimum reflectance axes values ($R_{MAX} > R_{INT} > > R_{MIN}$) and RIS-style parameter (R_{st}) (Ghosh et al. 2018).

4.3 Hydrocarbon generation properties

The TOC richness in low-medium rank coals from Meghalaya ranges from 35.31 wt% to 73.13 wt%, whereas it fluctuates between 59.24 wt% and 78.04 wt% in the medium-rank coals of the Raniganj and the Jharia Basins. The TOC values agree for good hydrocarbon generation potential. In favour, potentially liquid hydrocarbon generation can be expected from the Meghalaya coals based on their high hydrogen index (HI; avg. 307.90 mg HC/g TOC). This is supported by their persistent sulfur-rich (type-IIS) kerogen and higher genetic potential values. Moreover, the $\bar{R}r\%$ values for Meghalaya coals are also in good agreement to infer their early oil generation potential (Fig. 3a). On the other hand, in the medium-rank coals, the HI values show a significant decline to the range of type-II-III kerogen. This kerogen type may imply the mixed oil and gas generation potential of the Raniganj and Jharia coal. Due to a higher degree of organic metamorphism at the anthracite stage and the large degree of aromatic polycondensation, the organic matter would have exhausted its capacity for any hydrocarbon generation. The S2 values are extremely low (< 0.03), and the S2 curves appear as a hump in the pyrograms, which also leads to anomalous and unreliable T_{max} values. Therefore, the Rock–Eval parameters such as S1, S2, and T_{max} are not recognized in the studied high-rank samples.

Moreover, as a whole, the GP and HI values are sharply declining at $\bar{R}_r$ 0.50%, possibly due to the first coalification jump (Table. 3; Fig. 3b), implying the effects of sulfur-rich reactive organic matrix on the early hydrocarbon generation from these coals. Sulfur is the most predominant heteroatom attached to the macromolecular matrix of coals rich in type-IIS kerogen. This type of kerogen comprises a large number of alkyl chains associated with the kerogen nuclei by the S–S and the C–S bonds. These bonds have lower bond dissociation energy (65 kcal/mole) than the C–O (85.5 kcal/mole) and the C–C (83 kcal/mole) bonds, which dominate the chemical frameworks of other kerogen types. Due to the presence of these weaker bonds and, therefore, consequent reactive chemical framework, type IIS kerogen can expel

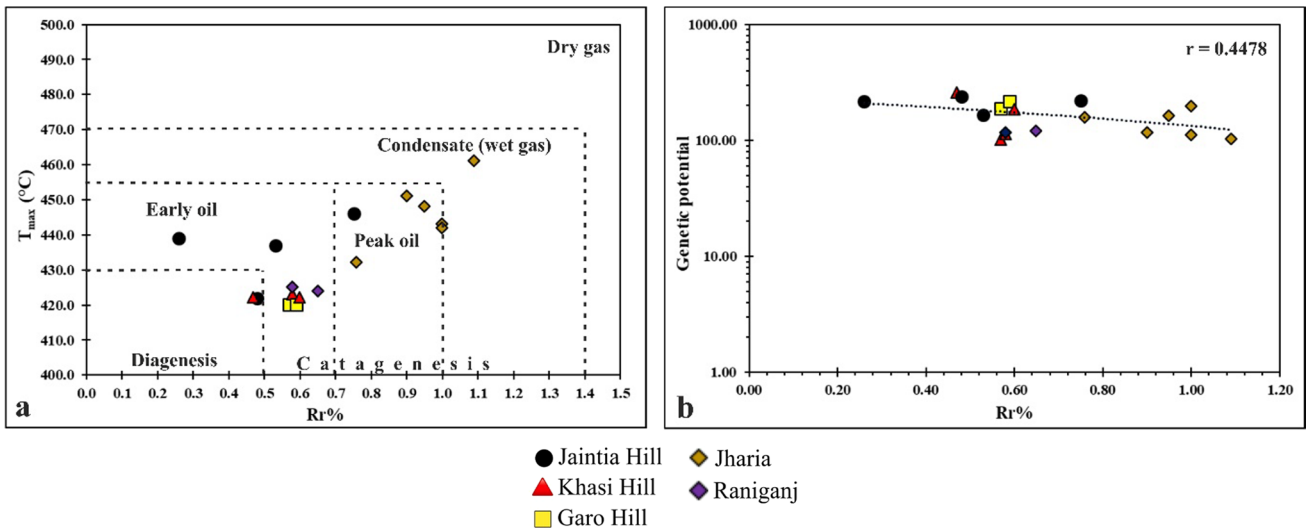

Fig. 3 **a** Mean random vitrinite reflectance ($\bar{R}_r\%$) vs. Temperature at which maximum hydrocarbon recorded under S2 curve (T_{max}) and **b** Mean random vitrinite reflectance ($\bar{R}_r\%$) vs. Genetic potential (S1 + S2)

Table 3 Hydrocarbon generation parameters calculated from Rock–Eval pyrolysis

Sample ID	Location	$\bar{R}_r$%	TOC (wt%)	S1 (mg HC/g rock)	S2 (mg HC/g rock)	T_{max} (°C)	HI (mg HC/g TOC)	GP (mg HC/g rock)
CG-5213	Jaintia Hills	0.26	58.39	12.21	204.18	439.00	350.00	216.39
CG-5219	Khasi Hills	0.47	73.13	6.89	250.77	422.00	343.00	257.66
CG-5209	Jaintia Hills	0.48	68.09	6.59	229.82	422.00	338.00	236.41
CG-5214	Jaintia Hills	0.53	52.86	5.29	158.79	437.00	300.00	164.08
CG-5221	Khasi Hills	0.57	38.52	2.13	98.28	420.00	255.00	100.41
CG-5227	Garo Hills	0.57	67.42	4.16	183.73	420.00	273.00	187.89
CG-5223	Khasi Hills	0.58	35.31	4.25	108.55	423.00	307.00	112.80
CG-5229	Garo Hills	0.59	64.55	5.03	211.12	420.00	327.00	216.15
CG-5217	Khasi Hills	0.60	60.18	6.35	179.01	422.00	297.00	185.36
CG-5204	Jaintia Hills	0.75	72.09	10.85	207.99	446.00	289.00	218.84
CG-1672	Raniganj	0.58	63.47	0.71	115.23	425.00	182.00	115.94
CG-1671	Raniganj	0.65	64.62	1.34	117.99	424.00	183.00	119.33
CG-1676	Jharia	0.76	59.29	3.17	154.82	432.00	261.00	157.99
CG-1675	Jharia	0.90	63.61	0.95	114.97	451.00	181.00	115.92
CG-1673	Jharia	0.95	78.04	1.63	159.55	448.00	204.00	161.18
CG-1677	Jharia	1.00	77.75	2.01	194.31	443.00	250.00	196.32
CG-1679	Jharia	1.00	59.24	1.64	109.39	442.00	185.00	111.03
CG-1674	Jharia	1.09	64.66	1.00	101.24	461.00	157.00	102.24

Explanations: $\bar{R}_r$% = Mean random vitrinite reflectance value; TOC (wt%) = Total Organic carbon; S1 = Expulsion of low-molecular-weight hydrocarbons under S1 curve in Rock–Eval pyrolysis (mg HC/g rock); S2 = Release of thermally cracked high-molecular-weight hydrocarbons recorded under S2 curve (mg HC/g rock); T_{max} (°C) = Maximum hydrocarbon liberation temperature recorded under S2 curve; HI = Hydrogen index: 100 × (S2/TOC) (mg HC/g TOC) ; GP = Genetic potential (S1 + S2) (mg HC/g rock)

hydrocarbons at a considerably lower temperature than the other kerogen types (Orr 1986). Type-IIS kerogen is, therefore, very reactive than type II-III kerogen that produces hydrocarbons before the peak thermal cracking of bitumen (Ma et al. 2016). Hence, the authors propose that the coalification jump in these samples occurs at the $\bar{R}_r$ of 0.50%. In support, it is suggested that during the coalification transition at $\bar{R}_r$ 0.50%, sulfur-containing functional groups, through reductive decomposition, may convert to H_2S, promoting hydrogen shuttling and, therefore, early cleavage of sulfur bonds. This process may help extract hydrogen from kerogen through free radical reactions (Trewhella and Grint 1987) and promote early oil generation.

4.4 Spectral demonstrations

4.4.1 Qualitative characterization of the functional groups

The fitted FTIR spectra are assigned to the specific functional groups following Ibarra et al. (1996), Coates (2006), Chen et al. (2012), Djomgoue and Njopwouo (2013), Okolo et al. (2015), Ghosh et al. (2020) and are presented in Table 4. In low to medium-rank coals from Meghalaya, the spectral deconvolution of the region 3700–3600 cm^{-1} reveals lucid –OH stretching vibrations of kaolinite, characterized by three peaks of surficial –OH group vibrations at ~ 3691, ~ 3678, and ~ 3658 cm^{-1} together with an inner surface vibration peak at ~ 3620 cm^{-1} (Fig. 4a) (Djomgoue and Njopwouo 2013). Whereas medium-rank coals from the Jharia and the Raniganj Basins coals depict three peaks at 3694 cm^{-1}, 3652 cm^{-1}, and 3620 cm^{-1} (Fig. 4b). On the other hand, only the inner surface hydroxyl group marks the kaolinite structure in the high-rank samples from the Rangit tectonic window (Fig. 4c). This transition may imply an increasing degree of dehydroxylation and progressive loss of the –OH group with coalification. Meanwhile, the inner surface –OH group would have stronger hydrogen bond energy to survive that process than the surficial species, making it the only prominent group in the high-rank coal samples from Sikkim (Ghosh et al. 2020). Further, all samples show IR absorbance of the pyrrolic –NH group with variable intensities. A cluster of peaks observed in the region of 3100–3000 cm^{-1} is assigned to the vibrations of aromatic C–H stretching due to the cross-linking aromatic structures (Cooke et al. 1986). In low to medium-rank coals of Meghalaya, spectral distribution observed in the region of 3000–2800 cm^{-1} is attributed to the aliphatic C–H stretching bonds resulting from the presence of the aliphatic side-chains (Chen et al. 2012). This region consists of several distinct peaks of the asymmetric and symmetric aliphatic $–CH_3$ and $–CH_2$

Table 4 Peak Assignments of the deconvoluted FTIR spectra of the studied samples following Ibarra et al. (1996), Coates (2006), Chen et al. (2012), Djomgoue and Njopwouo (2013), Okolo et al. (2015) and Ghosh et al. (2020)

Serial number	Wavenumber (cm^{-1})	Assignments
1	~3691	Kaolinite hydroxyl (–OH) stretching- surficial
2	~3678	Kaolinite hydroxyl (–OH) stretching- surficial
3	~3658	Kaolinite hydroxyl (–OH) stretching- surficial
4	~3620	Kaolinite hydroxyl (–OH) inner stretching- Inner surficial
5	~3510	Free –OH Group
6	~3458, ~3408, ~3366	Pyrrolic –NH
7	~3420	H–O–H stretching
8	~3400	Strong –OH group
9	~3319, ~3273	–OH ether O Hydrogen Bond
10	~3210	Tightly bound cyclic –OH tetramers
11	3100–3000	Aromatic C–H stretching
12	~2950	Asymmetric aliphatic CH_3 stretching vibration
13	~2920	Asymmetric aliphatic CH_2 stretching vibration
14	~2900 to 2880	R_3–CH stretching
15	~2870	Symmetric aliphatic CH_3 stretching vibration
16	~2850	Symmetric aliphatic CH_2 stretching vibration
17	~1730	Aromatic ester group (RCOOR') vibration
18	~1703	Vibrational intensity of aliphatic C=O and –COOH group
19	~1650	Aromatic C=O stretching
20	~1600	Aromatic C=C stretching
21	~1460	Aromatic C=C stretching
22	~1435	Aliphatic CH_2 and CH_3 bending vibrations
23	~1370	CH_3 symmetric bending vibration
24	~1350 to 1330	Aliphatic C–H in-plane bending vibration
25	~870	Aromatic nucleus C–H bending frequency with isolated aromatic hydrogen
26	~810	Aromatic nucleus C–H bending frequency with two to three adjacent aromatic hydrogen in each ring
27	~750	Aromatic nucleus C–H bending frequency with four (4) aromatic hydrogen
28	~695	Thiol or Thioether CH_2–S– (C–S stretch)
29	~630	Thioether CH_3–S– (C–S stretch)
30	~620, ~605	Disulfides (S–S stretch)
31	~595, ~580	Disulfides (C–S stretch)
32	~470	Polysulfides (S–S stretch)

Explanations: –CH_3= Methyl group; –CH_2= Methylene group; –OH= Hydroxyl group; RCOOR′= Aryl esters; –COOH= Carboxyl group; C=O= Carbonyl group; C–S= Carbon–Sulfur bond; S–S= Sulfur-Sulfur bond

stretching vibrations (Table 4). These peaks suggest that the studied low to medium-rank coal samples have a reactive aliphatic structure (straight-chain and branched) contributed mainly by the methylene and methyl groups. Nonetheless, the medium-rank samples from the Jharia and the Raniganj Basins illustrate only two prominent peaks of symmetric and asymmetric aliphatic –CH_2 stretching vibration (Ghosh et al. 2020). This may indicate the chemical transition within the coals during the first coalification jump and, therefore, may substantiate the authors' proposition to set the $\bar{R}_r$ value of 0.50% as the marker of the first coalification jump. However, the high-rank samples are devoid of the absorbance intensities in this region because of the coupling of thermal and stress degradation that prompted the expulsion of the aliphatic groups of low bond dissociation energy as hydrocarbons (Ghosh et al. 2020). Further, the absorption of infrared spectra at ~ 1730 cm^{-1} may indicate the presence of the aromatic ester group, while the influences of acid, ketones, and aldehydes on stretching vibrations of the aliphatic C=O and –COOH groups are recorded in the absorption peak of ~ 1703 cm^{-1} (Okolo et al. 2015). Moreover, C=O aromatic stretching vibrations are recorded at 1650 cm^{-1}. The peak detected at ~ 1600 cm^{-1} is attributed to the C=C aromatic stretching vibration of aromatic rings or aromatic nuclei. Further, the weakly intense peaks associated with the oxygenated functional groups (1750–1650 cm^{-1}) and aromatic

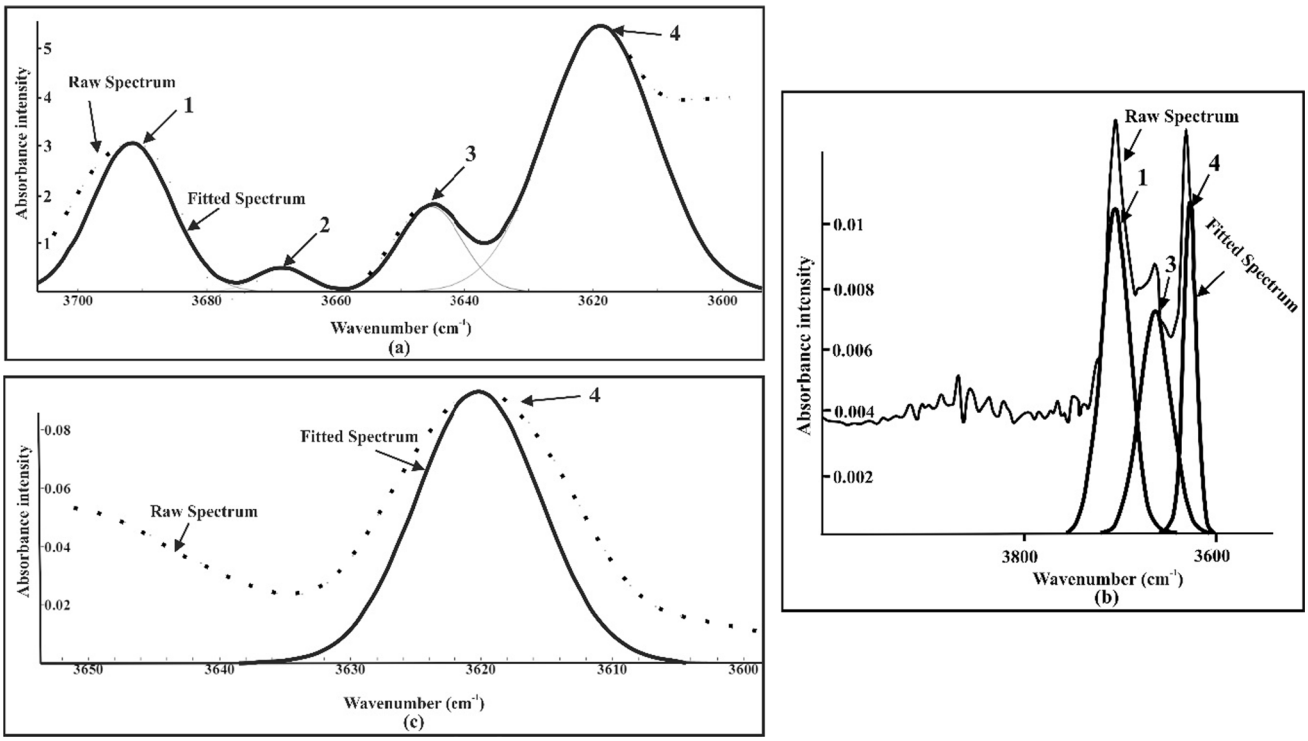

Fig. 4 Hydroxyl group (–OH) absorbance intensities of kaolinite in **a** CG-5204 (representative of the low to medium-rank coal samples from Meghalaya) and **b** CG-1679 (representative of the medium-rank coal samples from the Jharia and the Raniganj Basins), and **c** CG-3305 (representative of the high-rank samples from Rangit tectonic window). Reuse of Fig. 4b from Ghosh et al. (2020), with modification, is permitted by the Elsevier and Copyright Clearance center; Licence Number: 5215880419644; dated: 25th December 2021. Explanations: 1: Surficial –OH group vibration (3691 cm^{-1}); 2: Surficial –OH group vibration (3678 cm^{-1}); 3: Surficial –OH group vibration (3658 cm^{-1}); 4: Inner Surface –OH group vibration (3620 cm^{-1})

C=C stretching (1600 cm^{-1}) are found in the high-rank samples, possibly due to the increasing non-sensitivity of these functional groups to the IR spectra caused by a decrease in the net dipole moment.

Besides, the bending vibrations of the aliphatic $–CH_2$ and $–CH_3$ groups are recorded at ~ 1435 cm^{-1} in all the studied low to medium and medium-rank coal samples and only in one high-rank sample (CG-3300). This band may have a contribution from a few hydrogen-bonded –OH structures, but the peak at ~ 1460 cm^{-1} observed on the left shoulder of ~ 1435 cm^{-1} peak suggests a contribution from aromatic C = C stretching vibrations (Cooke et al. 1986; Coates 2006; van Niekerk et al. 2008; Okolo et al. 2015). The infrared absorption at ~ 1370 cm^{-1} is attributed to the presence of $–CH_3$ groups in aliphatic chains. Further, in low to medium-rank coals, aliphatic C–H in-plane bending vibrations are noted in the region between ~ 1350–1330 cm^{-1}. The high-rank samples are devoid of any peaks in this region due to the thermo-stress degradation effects. Further, the substitution of aromatic species in aromatic rings is indicated by aromatic out-of-plane C–H bending vibration from 900 to 700 cm^{-1} spectral regions (Fig. 5). This configuration may result from the Hydrogen-Carbon–Carbon (HCC) rocking vibration in the condensed aromatic ring system. Moreover, the absorbance intensities of the sulfur-containing structures are detected in the Meghalaya coals from 750 to 430 cm^{-1}, represented by thiol or thioether, disulfides (S–S, and C–S stretch), and the polysulfides (Fig. 6; Coates 2006).

4.4.2 Semi-quantitative characterization

The numerical parameters obtained from the IR spectra are shown in Table 5. Semi-quantitative characterizations of the infrared absorbance spectra are mainly performed based on the aliphatic carbon fraction (C_{al}/C), apparent aromaticity (f_a), "A-factor" and "C-factor". The apparent aromaticity (f_a) of lignite ($\bar{R}_r$: 0.40%) is 0.72; for subbituminous ($\bar{R}_r$: 0.40% & 0.50%) it is 0.74 and 0.77; for bituminous D ($\bar{R}_r$: 0.50%–0.60%), it ranges from 0.67 to 0.79, for bituminous C ($\bar{R}_r$: 0.60%–1.00%) it spans from 0.72 to 0.91, and for bituminous B ($\bar{R}_r$:1.00%–2.00%) it is 0.93. On the other hand, the apparent aromaticity (f_a) for high-rank samples falls between 0.96 and 1.00. The positive correlation between the f_a and $\bar{R}_r$ % in the low-rank coals ($r = 0.87$), low to medium-rank coals ($r = 0.77$), and

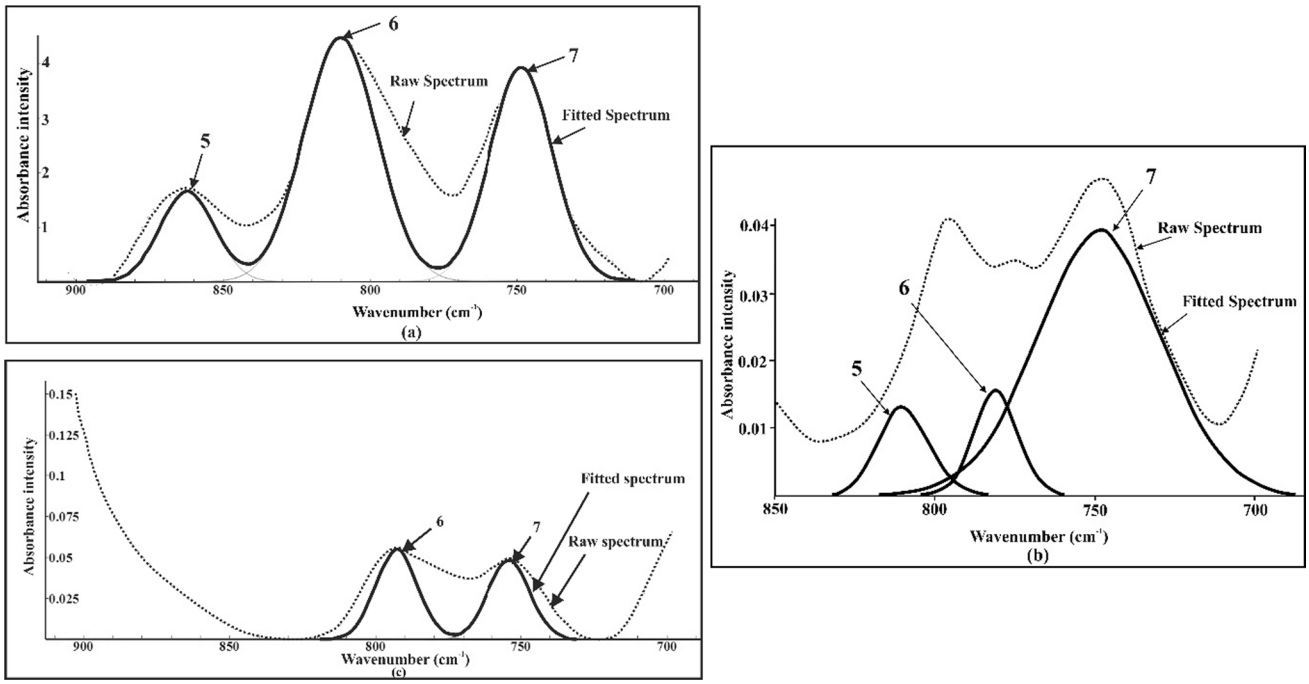

Fig. 5 Aromatic out-of-plane C–H bending frequencies in **a** CG-5204 (representative of the low to medium-rank coal samples from Meghalaya) and **b** CG-1679 (representative of medium-rank coal samples from the Jharia and the Raniganj Basins), and **c** CG-3305 (representative of the high-rank samples from the Rangit tectonic window). Explanations: 5: Aromatic C–H bending frequency with an isolated aromatic hydrogen atom (~870 cm^{-1}); 6: Aromatic C–H bending frequency with two to three aromatic hydrogen atoms (~810 cm^{-1}); 7: Aromatic C–H bending frequency with four adjacent aromatic hydrogen aromatic atoms (~750 cm^{-1})

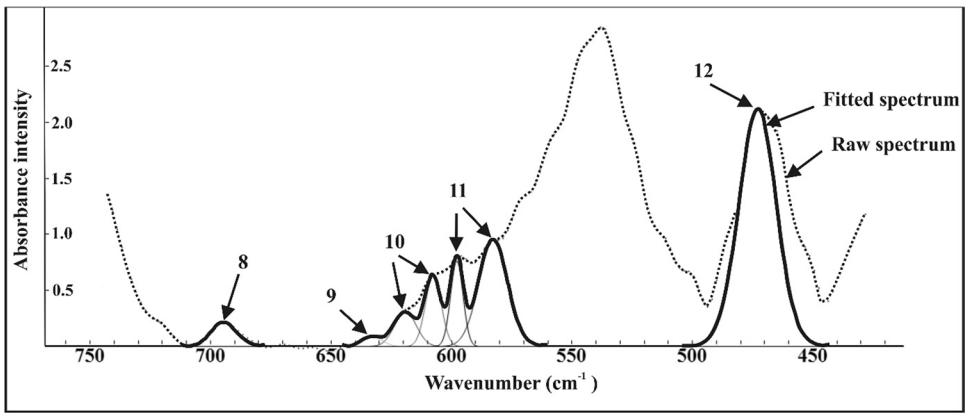

Fig. 6 Sulfur moieties in CG-5204 (representative of the low to medium-rank coal samples from Meghalaya). Explanations: 8: Thiol or Thioether CH_2–S– (C–S stretch) (695 cm^{-1}); 9: Thioether CH_3–S– (C–S stretch) (630 cm^{-1}); 10: Disulfides (S–S stretch) (620 and 605 cm^{-1}); 11: Disulfides (C–S stretch) (595 and 580 cm^{-1}); 12: Polysulfides (S–S stretch) (470 cm^{-1}) following Coates (2006)

for high-rank coals ($r = 0.82$) may indicate rising aromaticity with increasing coal rank due to thermo-stress polycondensation (Fig. 7a). The C_{al}/C shows the exact reverse trends with the rising vitrinite reflectance values (Fig. 7b). This substantial depletion in the aliphatic carbon fraction in the low, medium, and high-rank coal samples with the surging $\bar{R}_r$ parameter may imply the progressive elevation in the aromatization of the chemical framework with the gradual alleviation in the aliphatic compounds possibly due to their expulsion as hydrocarbons. These relations may, therefore, suggest a progressive growth in the condensed aromatic structures and stacked aromatic lamellae with lesser amounts of aliphatic side-chains and heteroaliphatic compounds with an increasing degree of coal metamorphism (Fig. 7). Interestingly, when all the coal samples from Meghalaya, Raniganj, and Jharia are plotted in a continuous series, these two indices depicted a weak correlation with the $\bar{R}_r$ parameter. However, the division of these coal samples into the low rank ($\bar{R}_r < 0.50\%$) and the medium rank ($\bar{R}_r > 0.50\%$), keeping the $\bar{R}_r$ value of 0.50% as the marker of the first coalification jump, enhances the statistical correlations between these two indices and the

Table 5 Semi-quantitative parameters from FTIR

Sample ID	Rank	$\bar{R}_r$ (%)	C_{al}/C	f_a	"C-factor"	"A-factor"
CG-5213	Lignite B	0.26	0.28	0.72	0.30	0.57
CG-5219	Sub-bituminous	0.47	0.26	0.74	0.80	0.79
CG-5209	Sub-bituminous	0.48	0.23	0.77	0.78	0.83
CG-5214	Bituminous D	0.53	0.24	0.76	0.89	0.87
CG-5221	Bituminous D	0.57	0.33	0.67	0.29	0.55
CG-5227	Bituminous D	0.57	0.29	0.71	0.82	0.89
CG-5223	Bituminous D	0.58	0.27	0.73	0.76	0.79
CG-5229	Bituminous D	0.59	0.29	0.71	nd	0.92
CG-5217	Bituminous D	0.60	0.31	0.69	0.78	0.91
CG-5204	Bituminous C	0.75	0.28	0.72	0.75	0.82
CG-1672	Bituminous C	0.58	0.21	0.79	nd	0.30
CG-1671	Bituminous C	0.65	0.26	0.74	nd	0.37
CG-1676	Bituminous C	0.76	0.23	0.77	nd	0.42
CG-1675	Bituminous C	0.90	0.23	0.77	nd	0.32
CG-1673	Bituminous C	0.95	0.16	0.84	nd	0.32
CG-1677	Bituminous C	1.00	0.24	0.76	nd	0.46
CG-1679	Bituminous C	1.00	0.09	0.91	nd	0.31
CG-1674	Bituminous B	1.09	0.07	0.93	nd	0.29
CG-3305	Anthracite A	4.15	0.04	0.96	nd	nd
CG-3306	Anthracite A	4.73	0.01	0.99	nd	nd
CG-3300	Anthracite A	5.12	0.00	1.00	nd	nd
CG-3303	Anthracite A	5.36	0.01	0.99	nd	nd

Explanation: ($\bar{R}_r$ %) Mean random vitrinite reflectance; nd-Not detected; $\bar{R}_r$% values for medium and high-rank coals are adopted from Ghosh et al. (2020). C_{al}/C = Aliphatic carbon fraction; f_a = Apparent aromaticity

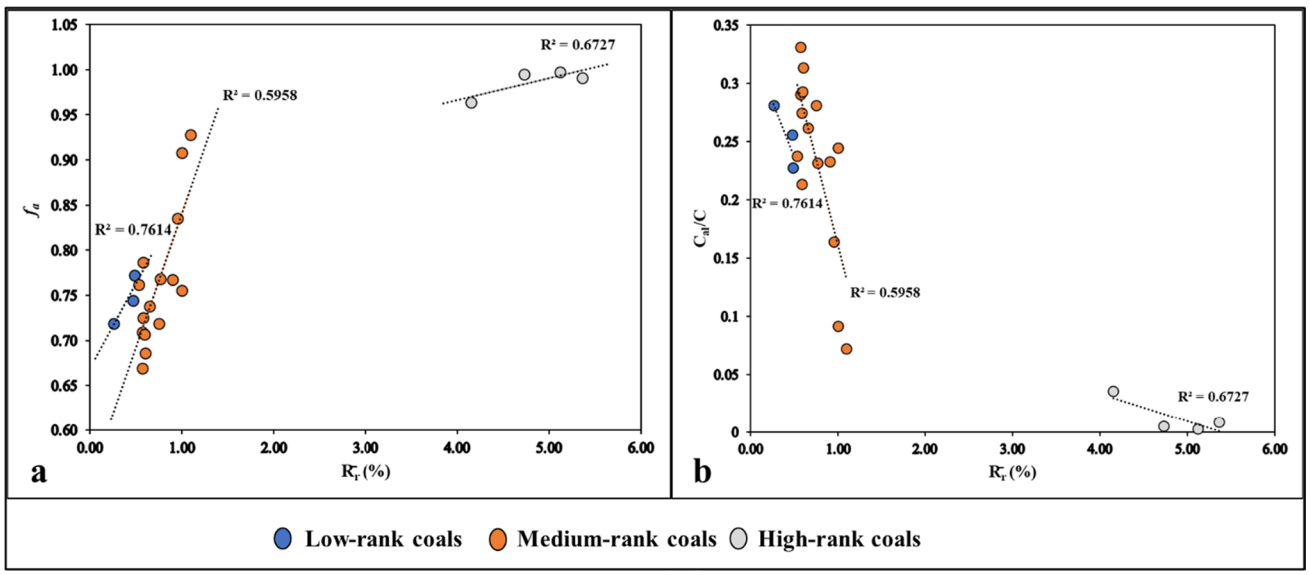

Fig. 7 Relation between the mean random vitrinite reflectance ($\bar{R}_r$ %) and the **a** apparent aromaticity and **b** aliphatic carbon with coalification

vitrinite reflectance. This may further support the author's observation that the coalification jump occurs earlier in the reactive organic matter at the sub-bituminous stage.

Moreover, the "A-factor" characterizes the reactivity of the chemical framework of organic matter based on the stretching of the labile aliphatic –CH functionalities

over the aromatic C=C stretching vibration. This index, although not precisely associated with the first coalification jump, sharply drops from the Meghalaya coal samples to the Raniganj and Jharia coals, which may indicate that the Meghalaya coal samples have a more reactive chemical framework capable of producing hydrocarbons earlier than the Raniganj and the Jharia coals at an early stage of thermal maturation.

4.4.3 Raman spectroscopy

Deconvolution of the Raman spectra exhibits bands associated with the amorphous and graphitic carbon furnished in Fig. 8. The quantitative Raman spectral parameters of the individual coal samples are summarized in Table 6. A perfectly ordered graphitic band that corresponds to the E_{2g2} vibration mode of the crystalline graphite moieties with the D_{6h}^4 symmetry at 1600 cm^{-1} is called the G band (Beyssac et al. 2002a, b; Li et al. 2006; Lahfid et al. 2010; Han et al. 2017; Xueqiu et al. 2017 and among others). This band originates from the vibration of the sp^2 hybridized C–C bond in aromatic structures (Henry et al. 2019a and 2019b). However, poor microstructural ordering introduces disorders in the crystalline structure, represented by the defect bands (D). These defect bands indicate highly disordered carbon structure around ~ 1150 cm^{-1} (S), 1350–1380 cm^{-1} (D_1), ~ 1500 cm^{-1} (D_3), ~ 1200 cm^{-1} (D_4), ~ 1260 cm^{-1} (D_5), and ~ 1440 cm^{-1} (D_6) in the first-order Raman spectra (Fig. 8a; Beyssac et al. 2002a, 2002b; Li et al. 2006; Lahfid et al. 2010; Ferralis et al. 2016; Han et al. 2017; Xueqiu et al. 2017; Henry et al. 2019a, 2019b). It is understood from the work of Li et al. (2006) that the peak around 1150 cm^{-1} corresponds to the S-band representing the vibrations of $C_{aromatic}$–C_{alkyl} ethers and C–C and C–H stretching

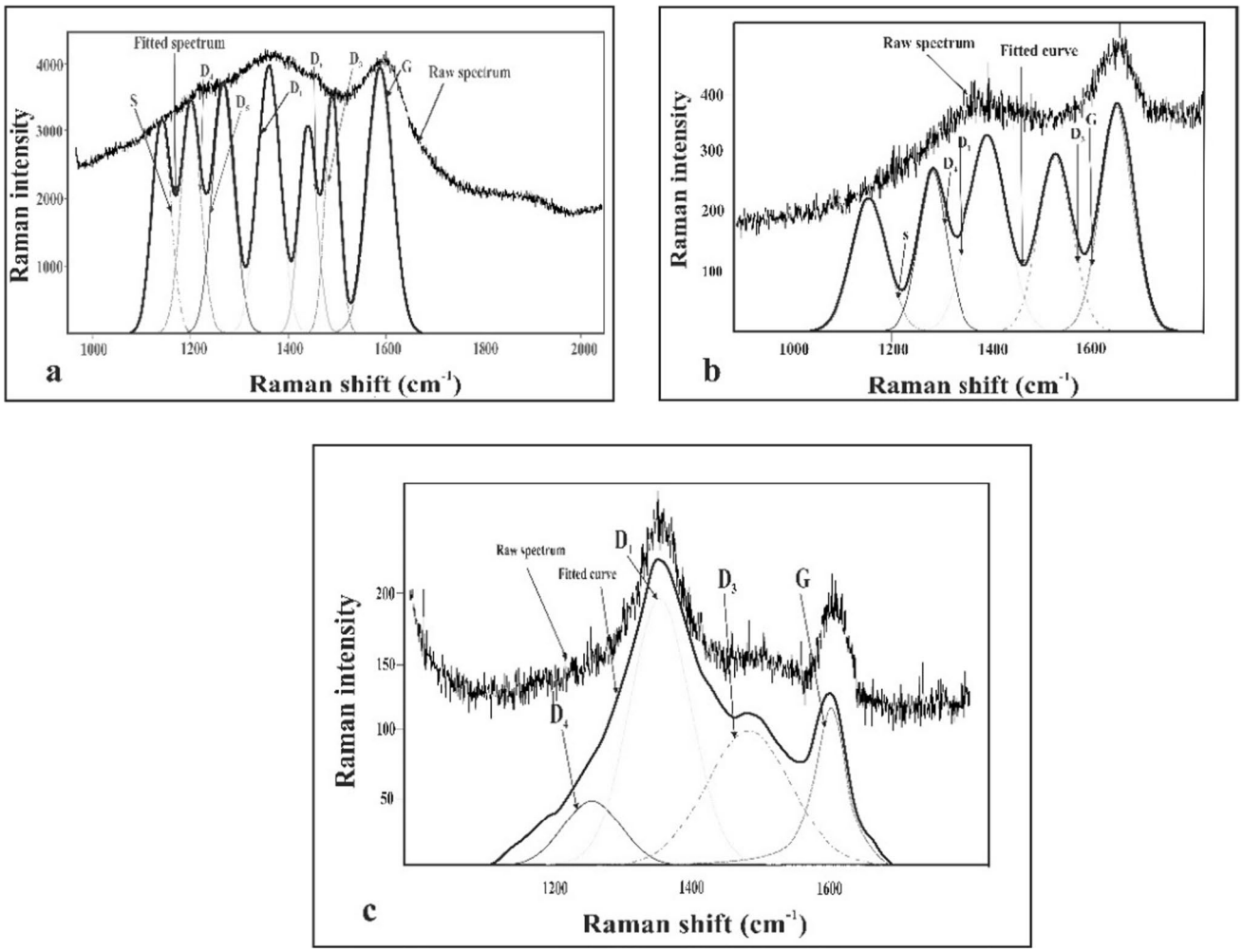

Fig. 8 Deconvoluted Raman spectra of **a** CG-5204 (representative for the low to medium-rank coal samples from Meghalaya), **b** CG-1679 (representative of medium-rank coal samples from the Jharia and the Raniganj Basins), and **c** CG-3306 (representative for high-rank samples from the Rangit tectonic window). Reusing Fig. 8b and c from Ghosh et al. (2020) is permitted by the Elsevier and Copyright Clearance center; Licence Number: 5215880419644; dated: 25th December 2021

Table 6 Quantitative parameters from the deconvoluted Raman spectra of the studied samples

Sample ID	Rank	$\bar{R}_r$ (%)	CD_1 (cm^{-1})	FWHM of D_1 (cm^{-1})	CD_3 (cm^{-1})	FWHM of D_3 (cm^{-1})	CD_4 (cm^{-1})	FWHM of D_4 (cm^{-1})	CD_5 (cm^{-1})	FWHM of D_5 (cm^{-1})	CD_6 (cm^{-1})	FWHM of D_6 (cm^{-1})	CS (cm^{-1})	FWHM of S (cm^{-1})	CG (cm^{-1})	FWHM of G (cm^{-1})	ID_1/IG	$G\text{-}D_1$
CG-5213	Lignite B	**0.26**	1360.51	52.83	1501.43	33.48	1202.4	18.75	1257.78	28.75	1447.27	24.13	1154.05	18.89	1587.53	42.3	1.01	227.02
CG-5219	Sub-bitumi-nous	**0.47**	1367.94	43.85	1502.29	29.38	1205.08	21.86	1264	35.63	1444.25	26.51	1162.58	25.19	1593.03	48.76	0.89	225.09
CG-5209	Sub-bitumi-nous	**0.48**	1370.37	49.92	1502.29	24.16	1202.05	19.83	1260.56	34.08	1440.37	28.25	1157.19	21.14	1592.03	43.53	0.91	221.66
CG-5214	Bitumi-nous D	**0.53**	1355.25	43.26	1502.71	23.2	1207.28	26.83	1264.88	26.42	1443.81	25.47	1153.12	17.23	1591.33	48.6	0.9	236.08
CG-5221	Bitumi-nous D	**0.57**	1364.44	57.83	1508.72	35.76	1207.3	23.19	1258.33	32.17	1448.13	31.17	1161.68	23.39	1581.61	45.69	0.96	217.17
CG-5227	Bitumi-nous D	**0.57**	1362.26	52.12	1502.29	37.99	1200.17	23.54	1267.11	56.69	1433.04	37.37	1154.95	29.59	1587.53	51.11	0.61	225.27
CG-5223	Bitumi-nous D	**0.58**	1372.72	38.19	1501.42	25.66	1202.82	23.92	1263.1	29.97	1436.48	25.73	1150.42	22.42	1593.87	52.39	0.88	221.15
CG-5229	Bitumi-nous D	**0.59**	1354.39	40.9	1503.14	35.23	1204.63	22.31	1255.56	29.85	1449.85	30.25	1150	28.01	1599.36	59.22	0.91	244.97
CG-5217	Bitumi-nous D	**0.6**	1374.48	50.23	1500.28	44.26	1205.08	20.97	1259.56	39.11	1438.22	31.98	1156.29	35.05	1587.96	46.49	0.92	213.48
CG-5204	Bitumi-nous C	**0.75**	1370.42	38.04	1506.15	26.41	1202.4	22.36	1262.23	20.73	1440.8	22.46	1150	22.08	1598.35	52.41	0.91	227.93
CG-1672	Bitumi-nous C	**0.58**	1408.79	108.98	1524.47	105.68	1260.29	84.54	nd	nd	nd	nd	1156.29	58.94	1646.14	110.4	0.85	237.35
CG-1671	Bitumi-nous C	**0.65**	1396.54	73.48	1496.5	99.96	1285.85	95.62	nd	nd	nd	nd	1134.52	51.32	1627.1	114.54	0.93	230.56
CG-1676	Bitumi-nous C	**0.76**	1398.22	111.78	1526.69	80.64	1287.54	101.22	nd	nd	nd	nd	1147.89	67.86	1652.94	92.32	0.84	254.72
CG-1675	Bitumi-nous C	**0.9**	1396.88	108.46	1520.58	135.14	1238.44	108.46	nd	nd	nd	nd	1116.24	83.42	1655.17	94.4	0.85	258.29
CG-1673	Bitumi-nous C	**0.95**	1396.02	124.02	1515.39	98.32	1263.64	74.02	nd	nd	nd	nd	1165.32	58.34	1620.75	104.04	0.93	224.73
CG-1677	Bitumi-nous C	**1**	1392.46	92.88	1529.48	80.78	1280.87	68.4	nd	nd	nd	nd	1153.5	83.98	1653.45	80.08	0.85	260.99
CG-1679	Bitumi-nous C	**1**	1391.03	53.88	1505.56	110.56	1292.55	88.44	nd	nd	nd	nd	1166.85	87.32	1657.95	80.7	0.79	266.92
CG-1674	Bitumi-nous B	**1.09**	1369.98	132.36	1507.83	130.4	1210.16	97.78	nd	nd	nd	nd	1106.03	59.42	1630.31	97.24	0.86	260.33

Table 6 (continued)

Sample ID	Rank	$\bar{R}_r$ (%)	CD_1 (cm^{-1})	FWHM of D_1 (cm^{-1})	CD_3 (cm^{-1})	FWHM of D_3 (cm^{-1})	CD_4 (cm^{-1})	FWHM of D_4 (cm^{-1})	CD_5 (cm^{-1})	FWHM of D_5 (cm^{-1})	CD_6 (cm^{-1})	FWHM of D_6 (cm^{-1})	CS (cm^{-1})	FWHM of S (cm^{-1})	CG (cm^{-1})	FWHM of G (cm^{-1})	ID_1/IG	G-D_1
CG-3305	Anthracite A	**4.15**	1363.42	76.95	1492.3	107.82	1293.04	72.92	nd	nd	nd	nd	nd	nd	1603.41	66.99	1.2	239.99
CG-3306	Anthracite A	**4.73**	1359.83	85.47	1486.91	137.29	1265.39	116.57	nd	nd	nd	nd	nd	nd	1608.36	55.18	1.58	248.53
CG-3300	Anthracite A	**5.12**	1357.93	64.79	1523.49	201.75	1257.44	131.62	nd	nd	nd	nd	nd	nd	1604.79	45.7	1.53	246.86
CG-3303	Anthracite A	**5.36**	1360.27	79.71	1487.41	112.15	1259.56	101.84	nd	nd	nd	nd	nd	nd	1604.91	64.21	1.98	244.64

Explanations: $\bar{R}_r$ (%) = Mean random vitrinite reflectance; $CD_1 = D_1$ band Centre; $CD_3 = D_3$ band Centre; $CD_4 = D_4$ band Centre; $CD_5 = D_5$ band Centre; $CD_6 = D_6$ band Centre; CG = Centre of G-band; CS = Centre S-band; ID_1/IG = Intensity ratio of D_1 to G; G-D_1 = Difference in the peak position of G to D_1 band; FWHM = Full width calculated at the half of the maximum band intensity. The $\bar{R}_r$% and the Centre of D_4, D_1, D_3, G, the FWHM-D_1; FWHM-G values along with ID_1/IG and AD_1/AG parameters related to the medium-rank and high-rank samples are adopted from Ghosh et al. (2020). Reuse of the Raman spectral parameters from Ghosh et al. (2020) for medium and high-rank samples from the Raniganj, Jharia, and Sikkim, India is permitted by the Elsevier and Copyright Clearance center; Licence Number: 5215880419644; dated: 25th December 2021

vibrations within the aromatic structures (Kuzmany et al. 2004; Ferralis et al. 2016). Meanwhile, the peak in 1350 to 1380 cm^{-1} range (D_1 band) corresponds to the structural disorders induced by the heteroatoms (Beny-Bassez and Rouzaud 1985). Meanwhile, Tunistra and Koeing (1970) proposed the origin of this band from the breathing of the sp^2 hybridized atoms in an aromatic ring with the A1g symmetry. In addition, the D_3 band, observed at ~ 1500 cm^{-1}, is a result of out-of-plane vibrations raised from the interstitial defects in the chemical structure of the organic material (Morga 2011; Baludikay et al. 2018; Henry et al. 2019a). This band may also arise from the interference of the poorly developed crystals within the internal lattice of organic matter (Beyssac et al. 2002a). Moreover, C–H stretching vibrations in the aliphatic hydrocarbon chains give rise to the D_4 and D_5 bands centred around ~ 1200 cm^{-1} and ~ 1260 cm^{-1}, respectively (Ferralis et al. 2016). Besides, the D_6 band at ~ 1440 cm^{-1} represents the trapped hydrocarbons within the micropores of organic matter. It was first recognized by Romero-Sarmiento et al. (2014).

The low to medium-rank coal samples from Meghalaya exhibit that all of these defect bands (D) are associated with the crystalline graphitic band (G), indicating a poorly organized microstructure. The small and under-developed crystallites, low degree of aromatic condensation, low aromaticity (supported by the FTIR spectra), and the abundances of aliphatic side-chains and labile hydrogen-bearing functional groups would have led to the disordered microstructural framework in these samples. Further, the presence of the D_6 band may indicate that reasonable amounts of early mature hydrocarbons are trapped within the micropores of the macerals suggesting the pre-catagenetic to a catagenetic phase of the thermal maturation. Thus, the presence of this particular band, along with the D_4 and D_5 bands, may support the highly reactive microstructure of the type II-S kerogen in these samples. Meanwhile, the medium-rank coal samples from the Jharia and the Raniganj Basins reveal the S, D_1, D_3, D_4, and G bands (Fig. 8b). The presence of the D_4 band, but the absence of the D_5 band may imply less reactive microstructure of type II–III admixed kerogen than the type II-S kerogen in the Meghalaya coal samples. Further, the absence of the D_6 band may indicate the peak catagenetic phase of thermal maturation, where the hydrocarbons are expelled from the organic micropores. However, in the high-rank samples from the Rangit tectonic window, only D_1, D_3, D_4, and G bands are observed (Fig. 8c), indicating relatively inert microstructure metagenesis to the post-metagenesis stage (anchizonal metamorphism) of thermal maturation. The defect bands in these samples are associated with the tetrahedral disorders that originated during the pre-graphitization phase, the introduction of microstructural defects by the Himalayan deformation episodes, and the presence of turbostratic carbon (Ghosh et al. 2018).

4.4.4 Semi-quantitative parameters of the Raman spectra

The microstructural disruptions in coal caused due to coalification, metamorphism, and deformation are determined using the Raman parameters such as intensity ratio (ID_1/IG), the difference in peak positions (G-D_1), and full width at half maximum (FWHM) (Table 6). The difference in peak positions between the G and D_1 bands (G-D_1) or the Raman band separation (RBS) has significant implications for determining the degree of microstructural ordering. The RBS values range from 213.48–244.97 cm^{-1}, 224.73–266.92 cm^{-1}, to 239.99–248.53 cm^{-1} for low to medium-rank Meghalaya coal samples, medium-rank coals from the Jharia and the Raniganj Basins, and high-rank samples from Sikkim, respectively. Among the low to medium-rank samples from Meghalaya, CG-5229 from the Garo Hills with the largest peak position difference may indicate a better microstructural ordering compared to the sample CG-5217 from the Khasi Hills with the least difference in the peak positions (Table 6). Likewise, the sample CG-1673 depicts the least peak position difference indicating a disordered microstructure. In contrast, sample CG-1679 illustrates a comparatively ordered microstructure with relatively large RBS among the medium-rank samples of the Jharia and the Raniganj Basins. Meanwhile, in the high-rank coal samples, the RBS parameter shows an insignificant variation, possibly suggesting almost similar microstructural characteristics (Table 6). However, in these samples, the RBS would have enhanced due to the shift of the D_1 band to the lower wavenumber as a result of high thermal maturity.

The ID_1/IG is another sensitive parameter that records the degree of graphitization and microstructural ordering in carbonaceous materials (Rahl et al. 2005; Rodrigues et al. 2011; Han et al. 2017; Schito et al. 2017, among others). This ratio initially declines up to 2.5% $\bar{R}_r$, then inclines up to the low-grade metamorphic stage, and then drastically depletes at the medium- to high-grade metamorphic phase until the microstructure becomes completely ordered (Beyssac et al. 2002a, b; Rahl et al. 2005; Lünsdorf et al. 2017; Henry et al. 2019a, b). Meanwhile, several authors observed an increase in the ID_1/IG ratio with the rising vitrinite reflectance (Guedes et al. 2010; Lahfid et al. 2010; Schito et al. 2017; Ghosh et al. 2020). Similar to these later observations, the ID_1/IG ratio in the studied low-rank coal samples from Meghalaya increases from the lignite to the subbituminous rank (r = 0.96; Fig. 9a), indicating an increasing degree of aromatic ring condensation (sp^2 hybridized atoms) and consequent improvement in the microstructural ordering with the rising degree of metamorphism. However, all the studied medium-rank coal samples exhibit a poor trend of this ratio with the $\bar{R}_r$ (%) parameter, which may indicate an almost similar metamorphic grade of these samples ($r = 0.06$; Fig. 9a). On the other hand, the high-rank samples show a strong positive trend between the $\bar{R}_r$ (%) and the ID_1/IG ratio due to an increased microstructural ordering ($r = 0.90$; Fig. 9a). Again, this may suggest an overall growth of the condensed aromatic structures with the rising vitrinite reflectance values at the anchizonal phase of metamorphism. This observation may also substantiate the escalation of the apparent aromaticity (f_a) in the high-rank samples. Hence, this ratio depicts a significant shift in the low-rank coals ($\bar{R}_r$: < 0.50%) but a poor trend in the medium-rank coals ($\bar{R}_r$ > 0.50%), suggesting that the ID_1/IG ratio is sensitive to the first coalification jump ($\bar{R}_r$: 0.50%), which is an interesting finding from this investigation. Further, this ratio shows a strong trend in the high-rank samples ($\bar{R}_r$: 4.15%–5.36%),

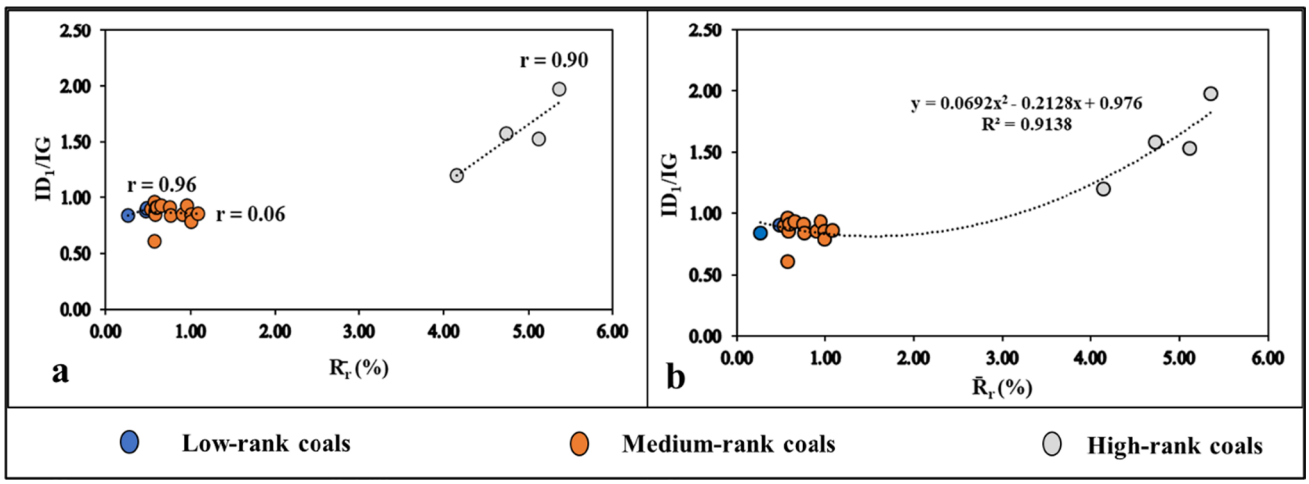

Fig. 9 **a** Variable responses of the intensity ratio of D_1 to G band (ID_1/IG) to the rising mean random vitrinite reflectance ($\bar{R}_r$%) values and **b** a polynomial trend of the ID_1/IG with the degree of coalification. Explanations: Some data points overlap in the reflectance range of the medium-rank coal samples

possibly indicating its sensitivity towards the anchizonal metamorphism and pregraphization phase of organic matter. So, a linear relationship does not fit all the data (ID_1/IG) throughout the reflectance ranges considered in this study, as this ratio responds differently to the reflectance ranges. Therefore, an effort is made to fit this ratio throughout the reflectance values of the low, medium, and high-rank coals. The authors have found that the ID_1/IG ratio and the mean random vitrinite reflectance ($\bar{R}_r$ %) values are best fitted with a quadratic polynomial trend (Eq. (7)) with the coefficient of regression (R^2) of 0.91 (Fig. 9b), which is also a novel observation from this investigation.

$$\frac{ID_1}{IG} = \left(0.0692 \times \overline{R}_r^2\right) - \left(0.2128 \times \overline{R}_r\right) + 0.976 \quad (7)$$

Besides, the FWHM of the G band was used extensively in the earlier investigations to estimate thermal maturity at $\bar{R}_r$% range from 0.5% to 3.0% (Kelemen and Fang 2001; Hinrichs et al. 2014; Romero-Sarmiento et al. 2014; Henry et al. 2019a, 2019b). Henry et al. (2019b) found a non-linear relation between the FWHM of the G band and the $\bar{R}_r$ % parameters. However, these two parameters barely show any linear relationship throughout the reflectance ranges of the studied coal samples. The non-linear shift of the G band-FWHM in the low and medium-rank coals may suggest that this parameter is less subtle to the transformations during the first coalification jump than the ID_1/IG ratio. Further, the G band usually shrinks with the increasing degree of coal metamorphism. However, in the studied high-rank samples from the Rangit tectonic window, it does not shrink, and its range (Table 6) may indicate the influence of tetrahedral defects and turbostratic carbon (Ghosh et al. 2018), which form during the pre-graphitization stage of the organic matter. Due to its intermediate stage of microstructural ordering between the amorphous and graphitic carbon, it may influence the FWHM of the graphitic band. Besides, the microstructural defects induced by the Himalayan orogeny would have hindered the complete growth of the graphitic crystalline structure in these samples resulting in the substantial width of the G band.

5 Hydrocarbon generation potential of the low to medium-rank coal samples: a glimpse from the semi-quantitative ratios

The FTIR spectroscopy can be efficiently applied to determine the type of kerogen present in the source rocks, its maturity, and assess the hydrocarbon potential. Similar to the van-Krevelen diagram constructed by the atomic H/C vs. atomic O/C ratios, Ganz and Kalkreuth (1987) used the "A-factor" and "C-factor" for determining kerogen type and maturation level of OM, respectively. The "A-factor" is a specific parameter for expressing the kerogen type, reactivity, and hydrocarbon generation potential of a source rock (Iglesias et al. 1995; Chen et al. 2012). This is calculated from the stretching vibrations of the aliphatic C–H functionalities. So, large concentrations of reactive aliphatic moieties may result in the larger aliphatic stretching, which raises the "A-factor". In all the studied Meghalaya coal samples, "A-factor" values ranging from 0.55 to 0.92 may suggest lower thermal maturity and promising hydrocarbon generation potential. Further, in the medium-rank coals of the Jharia and the Raniganj Basins, the "A-factor" value ranges from 0.29 to 0.46, which may point towards comparatively lower hydrocarbon potential of these medium-rank coals than the low to medium-rank Meghalaya coal samples. This further may substantiate the observations from the atomic H/C and O/C ratios. Besides, as discussed in subSect. 4.4.4, the presence of both D_4 and D_5 bands in the Meghalaya coals but the absence of the D_5 band in the Raniganj and the Jharia coal samples make the former samples more prone to hydrocarbon generation. Thus, the 'A-factor' parameter from the FTIR spectroscopy is in line with both the atomic ratios and Raman spectral features in assessing the hydrocarbon generation potential of the studied low to medium-rank coal samples.

Besides, the RBS (G-D_1 cm^{-1}), ID_1/IG, and the ratio of the full width at the half maxima of the D_1 to that of the G band (D_w/G_w) can be used in collaboration with the vitrinite reflectance to elucidate the thermal maturity and plausible types of hydrocarbon generation from the reactive kerogen (Sauerer et al. 2017; Tiwari et al. 2020; Adsul et al. 2021). These conjugated interrelations (Fig. 10) reveal that within the low-rank samples, the lignite is immature, while the sub-bituminous coals are at the pre-catagenetic phase. The medium-rank coals from Meghalaya are at the catagenesis stage to expel liquid hydrocarbons, while the Raniganj and Jharia coals are at the 'oil window' and trend towards the peak wet gas generation phase (post-catagenesis). Thus, these relations apparently exhibit significant oil potential of the Meghalaya coal samples (type II-S kerogen) but mixed oil and gas generation potential of the Raniganj and Jharia coals (type II-III admixed kerogen). Meanwhile, these observations from the FTIR and Raman semi-quantitative ratios require further validation from the lipid biomarker and micro-petrographic investigations to put forward sound conclusions.

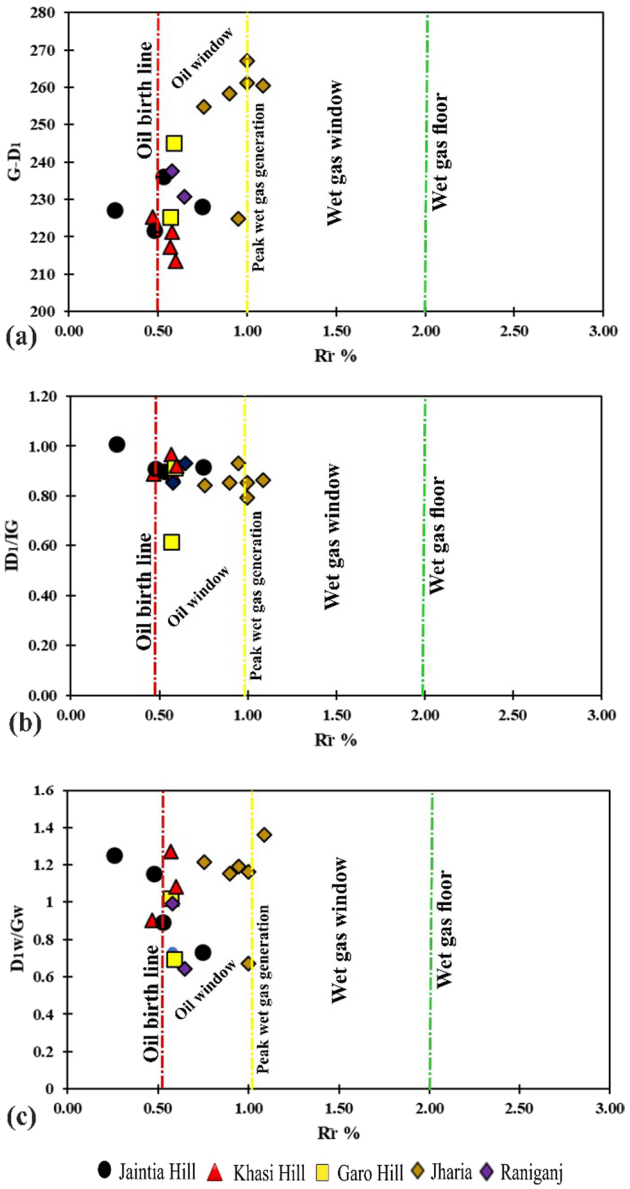

Fig. 10 Relation of the $\bar{R}_r$ % with the **a** G-D_1 band position difference, **b** intensity ratio of the D_1 and G bands, and **c** ratio of the full width at the half maxima of the D_1 and the G bands

6 Conclusions

The composite multispectral approach using the FTIR and Raman spectroscopy spectacularly portrays the whims of microstructural restyling during coalification and its controls on hydrocarbon generation. The spectral features exhibit a gradual depletion of the aliphatic moieties and enhancement of the apparent aromaticity with the increasing degree of coalification. Further, this apparent aromaticity responds to the first coalification jump at the $\bar{R}_r$: 0.50%, at the boundary between the low-rank ($\bar{R}_r$: < 0.50%) and medium-rank coals ($\bar{R}_r$: > 0.50%). Besides, the thermo-stress polycondensation of the aromatic structures enhances its values in high-rank coals. In support, the ID_1/IG ratio is also subtle to the first coalification jump and the pregraphitization phase of organic matter. Due to its variable responses to the coalification, this ratio reveals a quadratic polynomial relation with the vitrinite reflectance range from 0.26% to 5.36%. Moreover, the Rock–Eval hydrogen index and genetic potential also decline sharply at the first coalification jump. This investigation also reports the plausible influences of microstructural niceties on hydrocarbon generation from the studied coal samples. The atomic ratios, vitrinite reflectance values, and paleotemperature suggest that all the medium-rank coal samples are at the catagenetic phase (oil window) of thermal maturation. Besides, the presence of the presence of sulfur functionalities in the type II-S kerogen, D_4, and D_5 bands in the Raman spectra, along with the large "A-factor" values, mark the early mature oil generation for the Meghalaya coal samples. Further, the Raniganj and Jharia coals comprising admixed type II-III kerogen are at the catagenetic stage with a trend towards the peak wet gas generation phase. Hence, show a mixed hydrocarbon potential. Meanwhile, thermo-stress polycondensation in the high-rank coal samples possibly developed an inert microstructure with negligible potential to generate hydrocarbons at metagenesis to post-metagenesis phase.

Supplementary Information The online version contains supplementary material available at https://doi.org/10.1007/s40789-023-00591-8.

Acknowledgments Dr. Shimin Liu, the Editor-in-Chief, and three anonymous reviewers are thanked for their valuable comments that improved the quality of this manuscript. The authors are indebted to Mr. Ritam Konar from the Geological Survey of India (GSI) for providing the Meghalaya coal samples for this investigation. The samples were collected as a part of a collaborative research project between GSI and IIT (ISM) carried out as an annual program of GSI in 2019-20. The authors are thankful to the Department of Science and Technology (DST) India for sponsoring funds to the Department of Applied Geology, Indian Institute of Technology (Indian School of Mines), Dhanbad, India, to get equipped with technologically advanced instrumental facilities under the scheme of DST-FIST Level II [No- SR/FST/ES II014/2012 (C)].

Author contribution TA: Conceptualization, Investigation, Writing-original draft. SG: Data curation, Formal analysis. AO: Fieldwork. SB: Resources. AKV: Supervision, Writing-review and editing.

Declarations

Conflict of interest The authors declare that they have no known competing financial interests or personal relationships that could have appeared to influence the work reported in this paper. Moreover, the experiments performed comply with the current Indian laws.

References

Adsul T, Ghosh S, Varma AK (2021) Allusions of Raman spectroscopy on microstructural ordering and thermal maturity assessment of kerogen. In: An abstract volume published at 72nd International Committee for Coal and Organic Petrology (ICCP) at Prague, Czech Republic, Conference Proceedings. pp 15–16

Ahmed M, Bharali D (1985) Petrographic characters of tertiary coals, Nangwalbibra, West Daranggiri Coalfield, Meghalaya. In: Proc Vth Geophytol Conf, Lucknow, pp 242–245

Anwita, Ghosh S, Varma AK, Das SK, Pal D, Solanki G (2020) Metamorphic transformations of nitrogen functionalities: Stabilization of organic nitrogen in anthracite and its effect on δ15N parameter. J Mar Pet Geol 112:104090. https://doi.org/10.1016/j.marpetgeo.2019.104090

ASTM D3175-15 (2015) Standard practice for ultimate analysis of coke and coal. ASTM international, West Conshohocken, PA, USA, www.astm.org

Baludikay BK, François C, Sforna MC, Beghin J, Cornet Y, Storme JY, Fagel N, Fontain F, Littke R, Baudet D, Delvaux D, Javaux EJ (2018) Raman microspectroscopy, bitumen reflectance, and illite crystallinity scale: comparison of different geothermometry methods on fossiliferous Proterozoic sedimentary basins (DR Congo, Mauritania, and Australia). Int J Coal Geol 191:80–94. https://doi.org/10.1016/j.coal.2018.03.007

Barker CE, Goldstein RH (1990) Fluid-inclusion technique for determining maximum temperature in calcite and its comparison to the vitrinite reflectance geothermometer. Geology 18:1003–1006. https://doi.org/10.1130/0091-7613(1990)018%3c1003:FITFDM%3e2.3.CO;2

Barker CE, Pawlewicz MJ (1986) The correlation of vitrinite reflectance with maximum temperature in humic organic matter. In: Bunterbath G, Stegena L (eds) Paleothermics. SpringerVerlag, Berlin, Heidelberg, pp 79–93

Barker CE, Pawlewicz MJ (1994) Calculation of vitrinite reflectance from thermal histories and peak temperatures. In: Mukhopadhyay PK, Dow WG (eds) Vitrinite reflectance as a maturity parameter applications and limitations. American Chemical Society, pp 216–229

Baysal M, Yürüm A, Yıldız B, Yürüm Y (2016) Structure of some western Anatolia coals investigated by FTIR, Raman, ^{13}C solid-state NMR spectroscopy and X-ray diffraction. Int J Coal Geol 163:166–176. https://doi.org/10.1016/j.coal.2016.07.009

Bény-Bassez C, Rouzaud JN (1985) Characterization of carbonaceous materials by correlated electron and optical microscopy and Raman microspectroscopy. Scan Electron Microsc 1:119–132

Beyssac O, Goffé B, Chopin C, Rouzaud JN (2002a) Raman spectra of carbonaceous material in metasediments: a new geothermometer. J Metamorph Geol 20(9):859–871. https://doi.org/10.1046/j.1525-1314.2002.00408.x

Beyssac O, Rouzaud JN, Goffé B, Brunet F, Chopin C (2002b) Graphitization in a high-pressure, low-temperature metamorphic gradient: a Raman microspectroscopy and HRTEM study. Contrib Mineral Petrol 143(1):19–31. https://doi.org/10.1007/s00410-001-0324-7

Biswas S, Varma AK, Kumar M, Mani D, Saxena VK, Mishra V (2020) Influence of geochemical, organo-petrographical and palynofacies assemblages on hydrocarbon generation: a study from upper Oligocene coal and shale of the Makum Coal Basin, Assam, India. Mar Pet Geol 114:104206. https://doi.org/10.1016/j.marpetgeo.2019.104206

Bostick N, Cashman S, McCulloh T, Waddell C (1979) Gradients of vitrinite reflectance and present temperature in the Los Angeles and Ventura Basis, California. In: Oltz DF (ed) Low temperature metamorphism of kerogen and clay minerals. Society of Economic Paleontologists and Mineralogists, Loa Angeles, Pacific Section, pp 65–96

Bustin RM, Guo Y (1999) Abrupt changes (jumps) in reflectance values and chemical composition of artificial charcoals and inertinite rich coals. Int J Coal Geol 38:237–260

Chandra D, Mazumdar K, Basumallick S (1983) Distribution of sulphur in the tertiary coals of Meghalaya, India. Int J Coal Geol 3:63–75

Chen Y, Mastalerz M, Schimmelmann A (2012) Characterization of chemical functional groups in macerals across different coal ranks via micro-FTIR spectroscopy. Int J Coal Geol 104:22–33. https://doi.org/10.1016/j.coal.2012.09.001

Coates J (2006) Interpretation of infrared spectra, a practical approach. Encycl Anal Chem. https://doi.org/10.1002/9780470027318.a5606

Cooke NE, Fuller OM, Gaikwad RP (1986) FT-i.r. spectroscopic analysis of coals and coal extracts. Fuel 65(9):1254–1260. https://doi.org/10.1016/0016-2361(86)90238-3

Djomgoue P, Njopwouo D (2013) FT-IR spectroscopy applied for surface clays characterization. J Surf Eng Mater Adv Technol 3:275–282

Ferralis N, Matys ED, Knoll AH, Hallmann C, Summons RE (2016) Rapid, direct and non-destructive assessment of fossil organic matter via microRaman spectroscopy. Carbon 108:440–449. https://doi.org/10.1016/j.carbon.2016.07.039

Ganz H, Kalkreuth W (1987) Application of infrared spectroscopy to the classification of kerogen types and the evaluation of source rock and oil shale potentials. Fuel 66(5):708–711. https://doi.org/10.1016/0016-2361(87)90285-7

Ghosh S, Rodrigues S, Varma AK, Esterle J, Patra S, Dirghangi SS (2018) Petrographic and Raman spectroscopic characterization of coal from Himalayan fold-thrust belts of Sikkim, India. Int J Coal Geol 196:246–259. https://doi.org/10.1016/j.coal.2018.07.014

Ghosh S, Ojha A, Varma AK (2020) Spectral manifestations of coal metamorphism: Insights from coal microstructural framework. Int J Coal Geol 228:103549. https://doi.org/10.1016/j.coal.2020.103549

Goswami DND (1985) Macerals and low temperature tar of the Tertiary coals of Assam, Meghalaya and Nagaland. Geosci J VI(1):95–102

GSI (Geological Survey of India) (2019) Indian coal and lignite resources. Natural Energy Resources Mission-II B. p 41

Guedes A, Valentim B, Prieto AC, Rodrigues S, Noronha F (2010) Micro-Raman spectroscopy of collotelinite, fusinite and macrinite. Int J Coal Geol 83:415–422

Guo Y, Bustin RM (1998) Micro-FTIR spectroscopy of liptinite macerals in coal. Int J Coal Geol 36(3–4):259–275. https://doi.org/10.1016/S0166-5162(97)00044-X

Han Y, Wang J, Dong Y, Hou Q, Pan J (2017) The role of structure defects in the deformation of high-ranked their influence on the macromolecular structure. Fuel 206:1–9. https://doi.org/10.1016/j.fuel.2017.05.085

Hazra B, Varma AK, Bandopadhyay AK, Mendhe VA, Singh BD, Saxena VK, Samad SK, Mishra DK (2015) Petrographic insights of

organic matter conversion of Raniganj basin shales, India. Int J Coal Geol 150–151:193–209. https://doi.org/10.1016/j.coal.2015.09.001
Henry DG, Jarvis I, Gillmore G, Stephenson M, Emmings JF (2018) Assessing low-maturity organic matter in shales using Raman spectroscopy: effects of sample preparation and operating procedure. Int J Coal Geol 191:135–151. https://doi.org/10.1016/j.coal.2018.03.005
Henry DG, Jarvis I, Gillmore G, Stephenson M (2019a) A rapid method for determining organic matter maturity using Raman spectroscopy: application to carboniferous organic-rich mudstones and coals. Int J Coal Geol 203:87–98. https://doi.org/10.1016/j.coal.2019.01.003
Henry DG, Jarvis I, Gillmore G, Stephenson M (2019b) Raman spectroscopy as a tool to determine the thermal maturity of organic matter: application to sedimentary, metamorphic and structural geology. Earth-Sci Rev. https://doi.org/10.1016/j.earscirev.2019.102936
Hinrichs R, Brown MT, Vasconcellos MAZ, Abrashev MV, Kalkreuth W (2014) Simple procedure for an estimation of the coal rank using micro-Raman spectroscopy. Int J Coal Geol 136:52–58. https://doi.org/10.1016/j.coal.2014.10.013
Ibarra JV, Moliner R, Bonet AJ (1994) FT-i.r. investigation on char formation during the early stages of coal pyrolysis. Fuel 73(6):918–924. https://doi.org/10.1016/0016-2361(94)90287-9
Ibarra JV, Muñoz E, Moliner R (1996) FTIR study of the evolution of coal structure during the coalification process. Org Geochem 24(6–7):725–735. https://doi.org/10.1016/0146-6380(96)00063-0
Iglesias MJ, Jiménez A, Laggoun-Défarge F, Suárez-Ruiz I (1995) FTIR study of pure vitrains and associated coals. Energy Fuels 9(3):458–466. https://doi.org/10.1021/ef00051a010
ISO 11760 (International Organization for Standardization) (2005) Classification of Coals, 1st edn. Switzerland, Geneva
ISO 18283 (International Organization for Standardization) (2006) Hard coal and coke-manual sampling
ISO 3310-1 (International Organization for Standardization) (2000) Test Sieve—technical requirements and testing—part 1: test sieve of metal wire cloth
ISO 7404-2 (International Organization for Standardization) (2009a) Methods for the petrographic analysis of coal—part 2: methods for preparing coal samples
ISO 7404-5 (International Organization for Standardization) (2009b) Methods for the petrographic analysis of coal—part 5: method of determining microscopically the reflectance of vitrinite
Jiang J, Yang W, Cheng Y, Liu Z, Zhang Q, Zhao K (2019) Molecular structure characterization of middle-high rank coal via XRD, Raman and FTIR spectroscopy: implications for coalification. Fuel 239:559–572. https://doi.org/10.1016/j.fuel.2018.11.057
Jiang J, Zhang S, Longhurst P, Yang W, Zheng S (2021) Molecular structure characterization of bituminous coal in Northern China via XRD Raman and FTIR spectroscopy. Spectrochim Acta Part A Mol Biomol Spectrosc 255:119724. https://doi.org/10.1016/j.saa.2021.119724
Kelemen SR, Fang HL (2001) Maturity trends in Raman spectra from kerogen and coal. Energy Fuels 15(3):653–658. https://doi.org/10.1021/ef0002039
Kelemen SR, George GN, Gorbaty ML (1990) Direct determination and quantification of sulphur forms in heavy petroleum and coals: 1. X-ray photoelectron spectroscopy approach. Fuel 69:939–944
Khare P, Baruah BP (2010) Structural parameters of perhydrous indian coals. Int J Coal Prep 30(1):44–67. https://doi.org/10.1080/19392691003781616
Khatibi S, Ostadhassan M, Tuschel D, Gentzis T, Bubach B, Carvajal-Ortiz H (2018) Raman spectroscopy to study thermal maturity and elastic modulus of kerogen. Int J Coal Geol 185:103–118. https://doi.org/10.1016/j.coal.2017.11.008
Killops S, Killops V (2005) Introduction to organic geochemistry (paperback) 2nd edn. Geofluids. https://doi.org/10.1111/j.1468-8123.2005.00113.x
Kuzmany H, Pfeiffer R, Salk N, Günther B (2004) The mystery of the 1140 cm-1 Raman line in nanocrystalline diamond films. Carbon 42(5–6):911–917. https://doi.org/10.1016/j.carbon.2003.12.045
Kwiecinska B, Suárez-Ruiz I, Paluszkiewicz C, Rodriques S (2010) Raman spectroscopy of selected carbonaceous samples. Int J Coal Geol 84(3–4):206–212. https://doi.org/10.1016/j.coal.2010.08.010
Lahfid A, Beyssac O, Deville E, Negro F, Chopin C, Goffé B (2010) Evolution of the Raman spectrum of carbonaceous material in low-grade metasediments of the Glarus Alps (Switzerland). Terra Nova 22:354–360
Li X, Hayashi JI, Li CZ (2006) FT-Raman spectroscopic study of the evolution of char structure during the pyrolysis of a Victorian brown coal. Fuel 85(12–13):1700–1707. https://doi.org/10.1016/j.fuel.2006.03.008
Liu FJ, Wei XY, Fan M, Zong ZM (2016) Separation and structural characterization of the value-added chemicals from mild degradation of lignites: a review. Appl Energy 170:415–436. https://doi.org/10.1016/j.apenergy.2016.02.131
Liu X, Song D, He X, Nie B, Wang L (2019) Insight into the macromolecular structural differences between hard coal and deformed soft coal. Fuel 245:188–197. https://doi.org/10.1016/j.fuel.2019.02.070
Lünsdorf NK (2016) Raman spectroscopy of dispersed vitrinite—methodical aspects and correlation with reflectance. Int J Coal Geol 153:75–86. https://doi.org/10.1016/j.coal.2015.11.010
Lünsdorf NK, Dunkl I, Schmidt BC, Rantitsch G, von Eynatten H (2017) Towards a higher comparability of geothermometric data obtained by Raman spectroscopy of carbonaceous material. Part 2: a revised geothermometer. Geostand Geoanal Res 41:593–612
Marques M, Suárez-Ruiz I, Flores D, Guedes A, Rodrigues S (2009) Correlation between optical, chemical and micro-structural parameters of high-rank coals and graphite. Int J Coal Geol 77(3–4):377–382. https://doi.org/10.1016/j.coal.2008.06.002
Mishra HK, Ghosh RK (1996) Geology, petrology and utilisation potential of some Tertiary coals of the northeastern region of India. Int J Coal Geol 30(1–2):65–100. https://doi.org/10.1016/0166-5162(95)00038-0
Mishra S, Panda PP, Pradhan N, Satapathy D, Subudhi U, Biswal SK, Mishra BK (2014) Effect of native bacteria Sinomonas flava ^{1}C and Acidithiobacillus ferrooxidans on desulphurization of Meghalaya coal and its combustion properties. Fuel 117(Part A):415–421. https://doi.org/10.1016/j.fuel.2013.09.049
Misra BK (1992) Optical properties of some Tertiary coals from northeastern India: their depositional environment and hydrocarbon potential. Int J Coal Geol 20(1–2):115–144. https://doi.org/10.1016/0166-5162(92)90007-J
Misra S, Varma AK, Hazra B, Biswas S, Samad SK (2019) The influence of the thermal aureole asymmetry on hydrocarbon generative potential of coal beds: insights from Raniganj Basin, West Bengal, India. Int J Coal Geol 206:91–105. https://doi.org/10.1016/j.coal.2019.03.008
Morga R (2011) Micro-Raman spectroscopy of carbonized semifusinite and fusinite. Int J Coal Geol 87(3–4):253–267. https://doi.org/10.1016/j.coal.2011.06.016
Morga R, Jelonek I, Kruszewska K, Szulik W (2015) Relationships between quality of coals, resulting cokes, and micro-Raman spectral characteristics of these cokes. Int J Coal Geol 144–145:130–137. https://doi.org/10.1016/j.coal.2015.04.006

Okolo GN, Neomagus HWJP, Everson RC, Roberts MJ, Bunt JR, Sakurovs R, Mathews JP (2015) Chemical-structural properties of South African bituminous coals: Insights from wide angle XRD-carbon fraction analysis, ATR-FTIR, solid state ^{13}C NMR, and HRTEM techniques. Fuel 158:779–792. https://doi.org/10.1016/j.fuel.2015.06.027

Oliveira MLS, Marostega F, Taffarel SR, Saikia BK, Waanders FB, Daboit K, Baruah BP, Silva LFO (2014) Nano-mineralogical investigation of coal and fly ashes from coal-based captive power plant (India): an introduction of occupational health hazards. Sci Total Environ 468–469:1128–1137. https://doi.org/10.1016/j.scitotenv.2013.09.040

Orr WL (1986) Kerogen/asphaltene/sulfur relationships in sulfur-rich Monterey oils. Org Geochem 10(1–3):499–516. https://doi.org/10.1016/0146-6380(86)90049-5

Orrego-Ruiz JA, Cabanzo R, Mejía-Ospino E (2011) Study of Colombian coals using photoacoustic Fourier transform infrared spectroscopy. Int J Coal Geol 85(3–4):307–310. https://doi.org/10.1016/j.coal.2010.12.013

Painter PC, Coleman MM, Snyder RW, Mahajan O, Komatsu M, Walker PL (1981) Low temperature air oxidation of caking coals: fourier transform infrared studies. Appl Spectrosc 35(n):106–110. https://doi.org/10.1366/0003702814731842

Piedad-Sánchez N, Izart A, Martínez L, Suárez-Ruiz I, Elie M, Menetrier C (2004) Paleothermicity in the Central Asturian Coal Basin. North Spain Int J Coal Geol 58(4):205–229. https://doi.org/10.1016/j.coal.2004.02.001

Rahl JM, Anderson KM, Brandon M, Fassoulas C (2005) Raman spectroscopic carbonaceous material thermometry of low-grade metamorphic rocks: calibration and application to tectonic exhumation in Crete. Greece Earth Planet Sci Lett 240:339–354

Raja Rao CS (1981) Coalfields of India coalfields of northeastern India. Geol Surv India Bull Ser A 45(1):75

Rodrigues S, Suárez-Ruiz I, Marques M, Flores D, Camean I, García AB (2011) Development of graphite-like particles from the high temperature treatment of carbonized anthracites. Int J Coal Geol 85(2):219–226. https://doi.org/10.1016/j.coal.2010.11.007

Romero-Sarmiento MF, Rouzaud JN, Bernard S, Deldicque D, Thomas M, Littke R (2014) Evolution of Barnett Shale organic carbon structure and nanostructure with increasing maturation. Org Geochem 71:7–16. https://doi.org/10.1016/j.orggeochem.2014.03.008

Sadezky A, Muckenhuber H, Grothe H, Niessner R, Pöschl U (2005) Raman microspectroscopy of soot and related carbonaceous materials: spectral analysis and structural information. Carbon 43(8):1731–1742. https://doi.org/10.1016/j.carbon.2005.02.018

Saikia BK, Boruah RK, Gogoi PK (2009) A X-ray diffraction analysis on graphene layers of Assam coal. J Chem Sci 121(1):103–106. https://doi.org/10.1007/s12039-009-0012-0

Sauerer B, Craddock PR, AlJohani MD, Alsamadony KL, Abdallah W (2017) Fast and accurate shale maturity determination by Raman spectroscopy measurement with minimal sample preparation. Int J Coal Geol 173:150–157. https://doi.org/10.1016/j.coal.2017.02.008

Schito A, Romano C, Corrado S, Grigo D, Poe B (2017) Diagenetic thermal evolution of organic matter by Raman spectroscopy. Org Geochem 106:57–67

Singh MP, Singh AK (2000) Petrographic characteristics and depositional conditions of Eocene coals of platform basins, Meghalaya, India. Int J Coal Geol 42(4):315–356. https://doi.org/10.1016/S0166-5162(99)00045-2

Singh YR, Abbott MB, Arnold TE, Singh SP (2021) Early Eocene palynofloras and geochemistry from the Garo Hills in Meghalaya (India). Rev Palaeobot Palynol 292:104458. https://doi.org/10.1016/j.revpalbo.2021.104458

Swer S, Singh OP (2003) Coal mining impacting water quality and aquatic biodiversity in Jaintia Hill district. ENVIS Bull Himal Ecol 11(2):25–33

Talukdar B, Kalita HK, Baishya RA, Basumatary S, Sarma D (2016) Evaluation of genetic toxicity caused by acid mine drainage of coal mines on fish fauna of Simsang River, Garohills, Meghalaya, India. Ecotoxicol Environ Saf 131:65–71. https://doi.org/10.1016/j.ecoenv.2016.05.011

Tao S, Chen S, Tang D, Zhao X, Xu H, Li S (2018) Material composition, pore structure and adsorption capacity of low-rank coals around the first coalification jump: A case of eastern Junggar Basin, China. Fuel 211:804–815. https://doi.org/10.1016/j.fuel.2017.09.087

Taylor GH, Teichmuller M, Davis A, Diessel CFK, Littke R, Robert P (1998) Organic petrology. Gebruder Borntraeger, Berlin (704 pp)

Tiwari B, Ojha A, Ghosh S, Varma AK, Mendhe VA, Mondal A (2020) A composite microstructural and geochemical approach to quench the quest for hydrocarbon from Barren Measures shales of Jharia Basin, India. J Nat Gas Sci Eng 78:103310. https://doi.org/10.1016/j.jngse.2020.103310

Trewhella MJ, Grint A (1987) The role of sulphur in coal hydroliquefaction. Fuel 66(10):1315–1320. https://doi.org/10.1016/0016-2361(87)90175-X

Tunistra F, Koenig JL (1970) Raman spectrum of graphite. J Chem Phys 53:1126

Van Niekerk D, Pugmire RJ, Solum MS, Painter PC, Mathews JP (2008) Structural characterization of vitrinite-rich and inertinite-rich Permian-aged South African bituminous coals. Int J Coal Geol 76(4):290–300. https://doi.org/10.1016/j.coal.2008.08.014

Varma AK, Hazra B, Mendhe VA, Chinara I, Dayal AM (2015) Assessment of organic richness and hydrocarbon generation potential of Raniganj basin shales, West bengal, India. Mar Pet Geol 59:480–490. https://doi.org/10.1016/j.marpetgeo.2014.10.003

Xin F, Xu H, Tang D, Cao C (2022) Differences in accumulation patterns of low-rank coalbed methane in China under the control of the first coalification jump. Fuel 324:124657. https://doi.org/10.1016/j.fuel.2022.124657

Xueqiu He, Liu X, Nie B, Song D (2017) FTIR and Raman spectroscopy characterization of functional groups in various rank coals. Fuel 206:555–563. https://doi.org/10.1016/j.fuel.2017.05.101

Yao S, Xue C, Hu W, Cao J, Zhang C (2006) A comparative study of experimental maturation of peat, brown coal and subbituminous coal: Implications for coalification. Int J Coal Geol 66(1–2):108-118. https://doi.org/10.1016/j.coal.2005.07.007

Zhou Q, Zhao Z, Zhang Y, Meng B, Zhou A, Qiu J (2012) Graphene sheets from graphitized anthracite coal: preparation, decoration, and application. Energy Fuels 26(8):5186–5192. https://doi.org/10.1021/ef300919d

Zhou S, Liu D, Cai Y, Yao Y (2017) Effects of the coalification jump on the petrophysical properties of lignite, subbituminous and high-volatile bituminous coals. Fuel 199:219–228. https://doi.org/10.1016/j.fuel.2017.02.092

Zhou S, Liu D, Karpyn Z T, Cai Y, Yao Y (2018) Effect of coalification jumps on petrophysical properties of various metamorphic coals from different coalfields in China. J Nat Gas Sci Eng 60:63–76. https://doi.org/10.1016/j.jngse.2018.10.004